Metal Ion Oligomerization Inside Electrified Carbon Micropores and Its Effect on Capacitive Charge Storage

Jiaqi Wei, Lixiang Zhong, Huarong Xia, Zhisheng Lv, Caozheng Diao, Wei Zhang, Xing Li, Yonghua Du, Shibo Xi, Mathieu Salanne, et al.

Metal Ion Oligomerization inside Electrified Carbon Micropores and Its Effect on Capacitive Charge Storage

Jiaqi Wei, Lixiang Zhong, Huarong Xia, Zhisheng Lv, Caozheng Diao, Wei Zhang, Xing Li, Yonghua Du, Shibo Xi, Mathieu Salanne,* Xiaodong Chen,* and Shuzhou Li**

J. Wei, L. Zhong, H. Xia, Z. Lv, W. Zhang, X. Chen, S. Li
Innovative Centre for Flexible Devices (iFLEX), School of Materials Science and Engineering, Nanyang Technological University, 50 Nanyang Avenue, Singapore 639798, Singapore
E-mail: chenxd@ntu.edu.sg; lisz@ntu.edu.sg

J. Wei, M. Salanne
Sorbonne Université, CNRS, Physico-chimie des Electrolytes et Nanosystèmes Interfaciaux, PHENIX, F-75005 Paris, France
E-mail: mathieu.salanne@sorbonne-universite.fr

Z. Lv, X. Chen
Institute of Materials Research and Engineering, the Agency for Science, Technology and Research, 2 Fusionopolis Way, Innovis, #08-03, Singapore138634, Singapore

C. Diao
Singapore Synchrotron Light Source, National University of Singapore, 5 Research Link, Singapore 117603, Singapore

X. Li
Henan Key Laboratory of Diamond Optoelectronics Materials and Devices, Key Laboratory of Material Physics, Ministry of Education, School of Physics and Microelectronics, Zhengzhou University, Zhengzhou 450052, China

Y. Du
National Synchrotron Light Source II, Brookhaven National Laboratory, Upton NY, 11973 USA

S. Xi
Institute of Chemical and Engineering Sciences, 1 Pesek Road, Jurong Island, Singapore 627833, Singapore
E-mail: xi_shibo@ices.a-star.edu.sg

M. Salanne
Institut Universitaire de France (IUF), 75231 Paris Cedex 05, France

Keywords: electrochemistry, ion complex structure, ion solvation, supercapacitor, X-ray absorption spectroscopy

Abstract

Ion adsorption inside electrified carbon micropores is pivotal for the operation of supercapacitors. Depending on the electrolyte, two main mechanisms have been identified so far, the desolvation of ions in solvents and the formation of superionic states in ionic liquids. Here, it is shown that upon confinement inside negatively charged micropores, transition metal cations dissolved in water associate to form oligomer species. They are identified using in situ X-ray absorption spectroscopy. The cations associate one with each other via hydroxo bridging, forming ionic oligomers under the synergic effect of spatial confinement and Coulombic screening. The oligomers display sluggish dissociation kinetics and accumulate upon cycling, which leads to supercapacitor capacitance fading. They may be dissolved by applying a positive potential, so an intermittent reverse cycling strategy is proposed to periodically evacuate micropores and revivify the capacitance. These results reveal new insights into ion adsorption and structural evolution with their effects on the electrochemical performance, providing guidelines for designing advanced supercapacitors.

1. Introduction

Supercapacitors are high-power electrochemical energy storage devices for portable electronics and electric vehicles. They store energy at the interface between electrically charged electrodes and electrostatically adsorbed ions.[1] Porous electrodes with large specific surface area are therefore necessary to obtain a high energy density.[2] In particular, microporous carbons with tailored porosity below 2 nm have shown superior capacitive energy storage performance.[3] Indeed, micropores display charging mechanisms that differ from the prediction of traditional models because their limited space prevents the formation of a complete electrical double-layer.[4] Understanding ion adsorption inside carbon micropores and its relationship with the electrochemical performance holds the key for the development of supercapacitors.

In recent years, various theoretical,[4b, 5] and experimental,[6] methods have been developed to analyze the structure of adsorbed electrolytes and have revealed the complex nature of charge storage inside micropores. The pores are pre-filled with electrolytes before charging, which leads to charging mechanisms based on ion exchange rather than simple counter ion (with opposite charge to the electrode) adsorption.[4b, 6c-f] In some cases, the size exclusion between solvated ions and micropores is overcome by partial desolvation.[5b, 6d, 6f] In solvent-free ionic liquids, superionic state forms upon spatial confinement and Coulombic screening.[4b, 5a, 6i] The population and diffusion of ions have also been explored with their effects on charge storage discussed.[6e-j] Despite fruitful progress being made, direct observation of the ion solvation structure and packing inside carbon micropores remains challenging with the limited characterization capability of current approaches, which restricts investigations of ion–ion and ion–pore interactions as well as designs of electrolyte composition and electrode structure.[6a]

X-ray absorption spectroscopy (XAS) can directly probe the local structure of specific elements even in the absence of long-range ordering.[7] It is effective in analyzing the structure of many

metal ions in solution, and/or under spatial confinement.[8] Among the ionic species with good XAS capability, transition metal ions dissolved in water have attracted more attention in recent years for their applications in supercapacitors,[9] aqueous ion batteries,[10] as well as transition metal recycling,[11] etc. Understanding the structure and packing of these ions inside carbon micropores is therefore of high interest. In addition, such knowledge may also enlighten behaviors of other supercapacitor electrolytes with low electron excitation energies and complicated chemical structures, which are hardly analyzed by XAS.[7a, 12]

Here we reveal the reversible oligomerization of transition metal aqua ions inside electrified carbon micropores using in situ XAS (**Figure 1**a). During charging of supercapacitors, the cations are electrostatically adsorbed into negatively charged micropores. They associate with each other through hydroxo coordination bridges and form ionic oligomers rather than simply desolvate (Figure 1b). Operando analysis demonstrates reversible oligomerization processes upon charging and discharging the device, as well as sluggish dissociation kinetics of the oligomers. This leads to accumulation of oligomers inside micropores upon cycling and capacitance fading of the supercapacitor. Therefore, we insert opposite cycles between cycling periodically to evacuate micropores and revivify the capacitance.

2. Results and Discussion

2.1. Anomalous Cation-Cation Coordination inside Negatively Charged Micropores

We employ commercial microporous and mesoporous carbons as the active material to study the structure of adsorbed ions (Figure S1 and Table S1, Supporting Information). To fit with the transmission mode XAS, we customize commercial coin cells with polyamide windows (Figure 1a). The electrodes are designed in a disk–ring configuration with the separator also punched in the center, so that X-rays only penetrate the working electrode without interacting with the bulk electrolyte and counter electrode. The customized cell works appropriately with

aqueous electrolytes of transition metal cations and demonstrates comparable electrochemical performance with conventional cell configuration (Figure S2, Supporting Information), which guarantees it as an ideal platform for in situ analysis.

We first examine the structure of Ni aqua ions in 1.0 M $Ni(NO_3)_2$ electrolyte in contact with microporous carbon electrodes. Ni K edge normalized X-ray absorption near edge structure (XANES) (Figure 1c) shows identical spectra for the electrolyte, as-assembled cell, and cell at applied potential of 1.0 V (the polarity of the cell is defined by the polarity of the working electrode). The spectrum corresponds to octahedral $[Ni(H_2O)_6]^{2+}$ that is commonly seen in bulk electrolytes.[8b] A different spectrum is then obtained for the cell at −1.0 V: although the pre-edge and white line are identical to the others, the shoulder around 8366 eV becomes steeper and the oscillation between 8370 and 8415 eV is suppressed. The identical pre-edge and white line indicate consistent octahedral coordination geometry and divalent ion nature of Ni ions,[13] while the other features suggest changes in the ligand and/or local structure around them.[14] The spectral changes show resemblance to the spectrum of $Ni(OH)_2$, in which Ni^{2+} is octahedrally coordinated to OH^- and the octahedra are linked via edge-sharing mechanism.

To further understand the solvation structure of Ni^{2+}, we conduct extended X-ray absorption fine structure (EXAFS) analysis of the samples. As plotted in Figure 1d, all samples have nearly identical R-space peak at 1.61 Å corresponding to Ni–O first neighbor distance. This indicates stable hexacoordinate structure of Ni^{2+}. However, new peaks arise at 2.73 Å, 5.02 Å, and 5.78 Å for the −1.0 V cell, which correspond well to the typical Ni–Ni distances in $Ni(OH)_2$ (Figure S3, Supporting Information). The resemblance is also observed clearly in k-space (Figure S4, Supporting Information). Fitting the EXAFS spectrum with $Ni(OH)_2$ structure yields good agreement and a Ni–Ni coordination number around 3.5, indicating an average unit number larger than 8 (Figure S5 and Supporting Notes, Supporting Information). These results indicate

association of $[Ni(H_2O)_6]^{2+}$ and formation of $Ni(OH)_2$-like ionic oligomers inside negatively charged carbon micropores, which resembles the hydrolysis and olation of transition metal aqua ions that normally happen under elevated pH and/or temperature only.[15] To verify this, we perform O K edge XAS of the samples to analyze the solvation shell around Ni^{2+}. As shown in Figure 1e, the pre-edge region between 530 and 535 eV, which corresponds to electron excitation from O 1s orbital to O 2p–Ni 3d hybridized orbital, shows strong variations due to changes in O chemical environments.[12] The pre-edge peak for the as-assembled and 1.0 V cells is around 533 eV, which represents the O atom of H_2O molecules in $[Ni(H_2O)_6]^{2+}$, while $Ni(OH)_2$ has one peak around 534.5 eV representing O atoms of OH^-. The −1.0 V cell with both Ni aqua ions and ionic oligomers then demonstrates dual peaks at 532.5 and 534.5 eV with both ligands (H_2O and OH^-),[16] thus proving the formation of $Ni(OH)_2$-like oligomers.

The combined Ni and O K edge XAS analyses draw a clear picture of the Ni aqua ion oligomerization inside microporous carbon electrode. In contrast, mesoporous carbon electrodes with larger pores present much smaller Ni–Ni scattering peak under identical testing condition (Figure S6, Supporting Information). This demonstrates the importance of pore size for the oligomerization, which sets spatial confinement to ions that requires partial desolvation and/or oriented alignment.[6f, 6i] Nevertheless, spatial confinement is not the only driving force for the process, since both the as-assembled and 1.0 V microporous carbon cells that are also impregnated with Ni aqua ions show no change in their structure.[4b, 6k] Negative surface charges are necessary for screening the Coulombic repulsion between the cations and allowing them to get closer,[5a, 6i, 17] forming bridged structures. As such, the oligomerization is ascribed to the synergy of the small pore dimension and the negative surface charging, which provide spatial confinement and Coulombic screening to the cations, respectively.

2.2. Reversible oligomerization of transition metal aqua ions

To investigate the ion oligomerization as a function of the applied potential and ionic species, we conduct operando XAS analysis with simultaneous chronoamperometry charging from 0 to ±1.0 V with 0.1 V step on cells using different electrolytes. As illustrated in **Figure 2**a, e, the initial spectra of cells with 1.0 M $Ni(NO_3)_2$ electrolyte before charging show features of the ionic oligomer. This is ascribed to the oligomers formed during pre-cycling,[6e, 6l] which have sluggish dissociation kinetics due to their bulky size and low charge density and are thus trapped. The spectra shift towards the one for $Ni(OH)_2$ during negative charging, which indicates an increase in the oligomerization of Ni aqua ions. On the contrary, closer resemblance to the spectra of the electrolyte upon positive charging demonstrates dissociation of the ionic oligomers and thus good reversibility of the process. The two-structure transition nature of the oligomerization is further corroborated by the isosbestic points in the XANES spectra.[7c]

Apart from Ni aqua ions, similar oligomerization behavior for Mn, Co, and Zn aqua ions are also observed in cells with 1.0 M $Mn(NO_3)_2$ (Figure 2b, f), $Co(NO_3)_2$ (Figure 2c, g), and $Zn(NO_3)_2$ (Figure 2d, h) electrolytes. All the cations associate into ionic oligomers inside negatively charged working electrode and dissociate back upon positive charging, with reversible formation and destruction of the M–M peaks. The intermediate initial spectra of the cells after pre-cycling indicate similar sluggish dissociation kinetics for all the oligomers, while the isosbestic points unravel the two-structure transition nature. These behaviors suggest that ion oligomerization may be a universal behavior for transition metal aqua ions under the synergic effect of spatial confinement and Coulombic screening. Nevertheless, each ion has specific oligomerization mode depending on its properties. While Ni aqua ions associate with octahedral unit, Mn, Co, and Zn aqua ions are partially desolvated to form tetrahedral solvation structures, as shown by the decreased intensity of the M–O peaks (Figure 2f–h) and the ab initio XANES spectra (Figure S7 and Supporting Notes, Supporting Information). This is due to the

smaller octahedral–tetrahedral crystal field stabilization energy differences of $3d^5$ Mn^{2+}, $3d^7$ Co^{2+}, and $3d^{10}$ Zn^{2+} compared to $3d^8$ Ni^{2+}, which are more easily overcome and make tetrahedral solvation structure more stable inside negatively charged micropores.[18] In addition, Co, Ni, and Zn aqua ions show single M–O peak and edge-shared M–M peak upon oligomerization, while Mn aqua ion displays two peaks associated to Mn–H_2O and Mn–OH^- pairs as well as edge- and corner-shared Mn–Mn peaks due to Jahn–Teller distortion of the tetrahedral complex.[19]

To quantitatively analyze the oligomerization processes, we conduct linear combination fitting (LCF) and edge step calculation (Figure S8 and Supporting Notes, Supporting Information) to the spectra. **Figure 3**a shows the LCF results with the spectra of the electrolytes and cells at −1.0 V state as the end members representing aqua ions (1) and ionic oligomers (0), respectively. During negative charging, the fraction of components remains stable until around −0.4 V and then shifts towards ionic oligomers almost linearly for all cations, which indicates oligomerization of the cations at high negative potentials. Concentrations of the cation (Figure 3b) are also almost unchanged before 0.4 V and raises monotonically afterward, indicating ion adsorption in line with oligomerization. Upon positive charging, the spectra and concentration are fixed before 0.4 V and change steadily afterward. This represents destruction of the oligomers and repulsion of the cations at positive enough potentials. The small structure and concentration changes at low-potential regimes suggest reaction barriers for the processes and thus charge storage based on short-scale ion rearrangement and/or anion migration.[5b, 6c] The barriers are ascribed to ion–ion and ion–surface interactions,[6e, 6k] which are overcome once a large enough electronic charge accumulates on the carbon surface at high applied potentials.[6b, 6j, 6l, 17] Above this threshold, the oligomerization and migration of the cations increase and play more significant roles in the charge storage. These results indicate the possibility to tailor supercapacitor charging behaviors by controlling the potential window.

Apart from the cation-specific oligomerization behaviors, we also explore the anion-specific effect on the oligomerization process. Using Ni aqua ion as an example coupled with different oxyanions (ClO_4^-, NO_3^-, SO_4^{2-}), we observe the presence of 2.73 Å scattering peak independent of the anion used (Figure S9, Supporting Information), which rules out an origin based on cation–anion pairing since the size of the anion varies and further confirms the formation of Ni–Ni coordination instead. Nevertheless, the different peak heights with the ranking NO_3^- > ClO_4^- >> SO_4^{2-} suggest different degree of oligomerization. The composition and concentration changes further confirm the anion-specific effect with the same ordering (Figure 3c, d). The result indicates less Ni aqua ions adsorption and oligomerization for $NiSO_4$ electrolyte than $Ni(ClO_4)_2$ and $Ni(NO_3)_2$ electrolytes, which is attributed to the SO_4^{2-}–pore interaction and/or SO_4^{2-}–cation pairing inhibiting the adsorption and/or hydrolysis of the cations and thus the oligomerization.[20] Nevertheless, potential dependence of the processes is similar with different anions, indicating that the reaction barriers are not disturbed by the anion-specific effect.

To analyze the oligomerization process in more detail, we further conduct operando XAS with simultaneous cyclic voltammetry (CV) experiments on cells with 1.0 M $Ni(NO_3)_2$ electrolyte. **Figure 4**a, d show the CV curves, in which the first charging curves differ slightly from the others and demonstrate more energy consumption. This is commonly known as the "activation" process due to irreversible side reactions, etc.[21] Along with the CV, the Ni–Ni scattering peak at 2.73 Å fades away above 0.4 V and rises below −0.4 V during the first positive and negative charging, respectively (Figure 4b, e and Figure S10, Supporting Information). The changes are similar to the ones observed during chronoamperometry charging and suggest a similar oligomerization behavior between the two charging methods. The peak does not reform during the following positive cycles, which indicates no ion oligomerization inside positively cycled micropores and further highlights the necessity of negative charging. For the negatively cycled

cell, the Ni–Ni peak drops only partially during discharging, which confirms the sluggish dissociation kinetics. During the following cycles, the cell demonstrates almost linear oscillation of the Ni–Ni peak intensity without potential barrier due to the residual ionic oligomers that are large enough to facilitate further oligomerization.[22] The composition of Ni^{2+} solvation environment extracted from LCF (blue curves in Figure 4c, f) agree well with the EXAFS changes. Concurrently, the concentration (red curves in Figure 4c, f) shows huge jumps during the first positive and negative charging, which is due to the activation and suggest build-up of in-pore ion distributions for working supercapacitors.[6l, 21] The negligible concentration changes during the following discharging also indicate trapping of the oligomers and maintaining of the ion distributions as a result of the synergy effect of high potential and confinement, which suggest unsymmetric charging and discharging behaviors as well as capacitance fading of supercapacitors. After the first cycle, the concentration varies almost linearly with net decrease and increase for the positively and negatively cycled cell, which indicates the elimination of reaction barriers as well as further depletion or accumulation of Ni ions. These results suggest gradual accumulation of Ni aqua ions inside negatively charged carbon micropores with ion oligomerization, which could consume extra energy and lead to blockage of the pores,[21, 23] influencing further capacitive charge storage. Nevertheless, it is also of high interesting to utilize the ion oligomerization and accumulation mechanism in other capacitive technologies such as deionization and actuation.

2.3. Capacitance fading and revivification of carbon micropores

To explore the effect of ion oligomerization and accumulation on charge storage, the performance of customized microporous carbon cells with 1.0 M $Ni(NO_3)_2$ electrolyte are analyzed. As shown in **Figure 5**a, the specific capacitance gradually drops with galvanostatic cycling between 0 to −1.0 V, especially during the first 10 cycles. Contrarily, the Coulombic

efficiency raises with cycling. Along with the performance change, ionic oligomers are gradually developed inside carbon micropores (Figure 5b and Figure S11, Supporting Information). The kinetics of ion oligomerization and accumulation is faster for the first 10 cycles than for the following cycles, which aligns well with the performance change. These results suggest strong correlations between the electrochemical performance and the ion oligomerization. Considering the ion oligomerization as an energy-consuming process,[23] the sluggish dissociation kinetics leads to accumulation of ionic oligomers inside micropores upon cycling (Figure 5c), which hinders further ion adsorption and oligomerization, reducing the capacitance in the following cycles.[6l, 21] The relatively freer micropores during initial cycles show stronger ion oligomerization with lesser dissociation (Figure 4d–f), thus resulting in higher capacitance but also severer fading and poorer Coulombic efficiency.

Based on the above analysis, we hypothesized that evacuating filled micropores with positive charging can restore the charge storage capability of supercapacitors. Therefore, we develop an intermittent reverse cycling method by inserting 5 opposite cycles between every 50 cycles. The opposite cycles effectively destruct ionic oligomers and restore the Ni^{2+} concentration back to the as-assembled state (Figure 5b). Meanwhile, the specific capacitance is also restored to the initial level (Figure 5a). With the intermittent method, we obtain a 95% capacitance retention through 600 cycles, compared to 86% with normal continuous method. Conversely, the intermittent method has no effect on the cycling performance between 0 to −0.4 V and 0 to 1.0 V (Figure S12, Supporting Information) due to the absence of ion oligomerization and thus accumulation, which further confirms the interference of these two processes to charge storage. Nevertheless, the low Coulombic efficiency is also restored together with the high specific capacitance because of the severe ion oligomerization and accumulation inside fresh micropores, and the capacitance fades again. The intermittent reverse cycling also works for alkali and alkaline earth metal ion aqueous electrolytes (Figure S12, Supporting Information),

which implies similar ion trapping for these electrolytes and proves the universality of our method. Another strategy to enhance the capacity retention is to use SO_4^{2-}-based electrolyte, which shows less ion oligomerization and thus less capacitance fading compared to other electrolytes (Figure S12, Supporting Information). However, $NiSO_4$ electrolyte also brings smaller specific capacitance due to lesser ion adsorption and oligomerization.[20c] These results suggest that further optimization of the capacitive charge storage should rely on elimination of the ion accumulation inside carbon micropores, such as by developing ionophobic carbons and advanced electrolytes, etc.

3. Conclusion

In conclusion, we reveal the reversible oligomerization of transition metal aqua ions inside electrified carbon micropores using in situ XAS. During charging of supercapacitors, the cations associate into ionic oligomers inside negatively charged micropores via hydroxo bridging under the synergy of spatial confinement and Coulombic screening. Contrarily, positive charging destructs the oligomers and repulses the cations. Each cation demonstrates specific structural evolution upon oligomerization depending on its properties, while an anion-specific effect on the degree of cation adsorption and oligomerization is discovered. Operando analysis with simultaneous CV cycling demonstrates sluggish dissociation kinetics and accumulation with cycling of the oligomers, which are responsible for the reduced charge storage capability. Based on these observations, we design an intermittent reverse charging method that revivifies the filled carbon micropores and leads to enhanced cycling performance. Our results demonstrate new insights into ion structural evolutions and their effects on capacitive charge storage, thus stimulating the design of advanced supercapacitor electrolytes and electrodes. The oligomerization of transition metal cations under nanoconfined electrical

stimulation also provides key information for the development of various electrochemical systems, such as aqueous ion battery, capacitive deionization, and electrochemical synthesis.

4. Experimental Section

Materials: Microporous carbon XFP-01 (average pore size 2.0–2.2 nm, specific surface area 1800±100 m^2 g^{-1}, purity ≥ 95%) and mesoporous carbon CMK-3 (average pore size 3.8–4.0 nm, specific surface area ≥ 900 m^2 g^{-1}, purity ≥ 99.6%) were purchased from Nanjing XF NANO Materials Tech Co., Ltd. Polyvinylidene fluoride (PVDF, Kynar® 761) was purchased from Arkema Inc. Manganese nitrate tetrahydrate ($Mn(NO_3)_2{\cdot}4H_2O$, > 97%), cobalt nitrate hexahydrate ($Co(NO_3)_2{\cdot}6H_2O$, 99.999%), zinc nitrate hexahydrate ($Zn(NO_3)_2{\cdot}6H_2O$, 98%), nickel nitrate hexahydrate ($Ni(NO_3)_2{\cdot}6H_2O$, 99.999%), nickel sulfate hexahydrate ($NiSO_4{\cdot}6H_2O$, 99.99%), nickel perchlorate hexahydrate ($Ni(ClO_4)_2{\cdot}6H_2O$, ≥ 98.0%), nickel hydroxide ($Ni(OH)_2$), and N-Methyl-2-pyrrolidone (NMP, anhydrous, 99.5%) were purchased from Sigma-Aldrich Inc. Conductive carbon black (super P, TIMCAL) was purchased from Imerys Graphite & Carbon Switzerland Ltd. All chemicals were used as received. De-ionized water (18.2 MΩ) was used for the preparation of the electrolytes.

Carbon Characterizations: Field emission scanning electron microscopy (FESEM, JEOL JSM-7600F) was used to study the morphology of carbon materials. N_2 gas sorption carried out at −195.85 °C with accelerated surface area and porosimetry system (TriStar ASAP 2020) was used to analyze the porosity of carbons and their electrodes. Samples were degassed at 120 °C, 5 μmHg overnight before tests to remove residual water. The specific surface area of the samples was calculated using the Brunauer–Emmett–Teller (BET) equation in the relative pressure of 0.05–0.25 as well as the original DFT model with slit pore. Pore size distribution was analyzed using the original DFT model with slit pore.

Electrode Fabrication and Cell Assembly: XFP-01 was used as the active material for studies and CMK-3 was selected as the control group. To fabricate the electrode, the active material (180 mg) was mixed with the binder (PVDF, 10 mg) and conductive additive (super P, 10 mg) and uniformly mixed in NMP (1200 μL) to form a homogeneous slurry. The slurry was pasted on aluminum foil using a doctor blade and was then dried in a vacuum oven (Anhua Inc.) at 60 °C for 2 hours followed by 120 °C overnight to fully remove the solvent. The dried electrode was compressed using a hydraulic press (MTI Inc.) with 10 KPa pressure to reach a condensed film with a final density ~15.0 mg cm^{-2}.

Customized CR2032 coin cell with a hole of 5.0 mm diameter at the center of both cases and spacers was used for all electrochemical tests and transition metal K edge XAS measurements. To assemble the cell, the electrode was cut into a round disk of 6.5 mm diameter as the examined "working electrode", and a ring with 6.5 mm/13.0 mm inner/outer diameters as the "counter electrode". Cellulose separator (TF4050, NKK Co., Ltd.) with 16.0 mm diameter and 4.0 mm diameter hole at the center was used. 30 μL 1.0 M aqueous electrolyte of one of the transition metal salts was added. The holes on both sides of the coin cell were sealed by polyamide tape followed by epoxy glue after cell assembly. Two copper wires were connected to the two sides of the coin cell as conducting extensions for electrochemical tests. Cells were rested for 10 hours before electrochemical tests.

Electrochemical Energy Storage Tests: The polarity of potentials applied to cells during electrochemical tests was defined by the polarity of potentials on the working electrode. Before testing, cells were activated by 5 cycles of positive galvanostatic charging/discharging (GCD) and then 5 cycles of negative GCD between 0 to 1.0 or −1.0 V with 0.2 mA current to avoid scattering from irreversible side reactions during the initial cycles.[21] For Ni K edge XAS of cells at fixed potentials, the cells were galvanostatically charged to ±1.0 V with 0.2 mA current and kept at the potential for 1 hour. For operando transition metal K edge XAS tests, chronoamperometry charging between 0 to ±1.0 V with 0.1 V step size and 18 minutes step

time, as well as CV scanning between 0 to ±1.0 V with 0.25 mV s^{-1} sweep speed were employed. For cycling tests, the cells underwent either normal continuous GCD, or intermittent GCD with 5 cycles of opposite GCD in between every 50 cycles. The current for cycling tests was 0.5 mA. The specific capacitance of cells during cycling test was calculated by integrating the charging/discharging curves with time.[24] The potential distribution on the working and counter electrodes was analyzed by measuring the potential of the working electrode during positive and negative GCD using a Ag/AgCl reference. GCD and CV were performed on an electrochemical workstation (Solartron 1470E, AMETEK Inc.), while chronoamperometry was performed on a battery analyzer (BTS4000, NEWARE technology Ltd.).

Transition Metal K Edge XAS: In situ transition metal K edge XAS were performed at the X-ray Absorption Fine structure for Catalysis (XAFCA) beamline of Singapore Synchrotron Light Source (SSLS) center.[7b] The customized cell was loaded on the sample holder with the polyamide window facing the transmission X-ray pathway. The copper wire extensions were connected to the battery analyzer next to the beamline to carrier out simultaneous electrochemical tests. The signal was measured between 6420 to 7100 eV, 7590 to 8310 eV, 8210 to 8930 eV, and 9540 to 10460 eV for Mn, Co, Ni, and Zn K edge, respectively, with ~0.9 eV energy step using flying scan mode. At least 2 sequential scans were recorded and merged for each sample/state, except for the operando analysis with CV cycling. The XAS data were processed using the Athena and Artemis software developed by Ravel and Newville.[25]

O K edge XAS: The as-assembled cell and cells at ±1.0 V were disassembled and their working electrodes were delivered to the Soft X-ray–Ultraviolet (SUV) beamline of SSLS center together with $Ni(OH)_2$ powder for O K edge XAS analysis.[26] The electrodes were stabilized in ultrahigh vacuum (10^{-8} Pa) overnight before test. Total electron yield mode soft XAS was conducted in 520–555 eV for O K edge measurement, with 0.1 eV energy step.

Supporting Information

Supporting Information is available from the author.

Acknowledgements
This work was supported by Singapore Ministry of Education Academic Research Fund Tier 2 (Grant No. MOE-T2EP10220-0005), Academic Research Fund Tier 1 (Grant No. RG104/18), Singapore National Research Foundation (Nanomaterials for Energy and Water Management CREATE Programme), Energy Innovation Research Programme (EIRP) (Grant No. NRF2015EWT‐EIRP002‐008), and French National Research Agency (Labex STORE-EX, Grant No. ANR-10-LABX-0076). The authors appreciate the soft XAS measurements from Soft X-ray–ultraviolet beamline, Singapore Synchrotron Light Source, and computing resources from National Supercomputing Singapore. The authors are grateful to Drs. Anne-Laure Rollet, Lin Liu, Yuxin Tang, Yao Xiao, and Zhiqiang Zhu, for helpful discussion.

Conflict of Interest
The authors declare no conflict of interest.

Author Contributions
J.W. carried out the experiments, being in main charge of this research. J.W., M.S., X.C., and S.L. prepared the manuscript. L.Z. conducted DFT calculations of the structures. J.W., Z.L., C.D., Y.D., and S.X. developed in situ XAS measurements and analyzed the data. S.X. performed FDMNES simulations. J.W., L.Z., H.X., C.D., X.L., Y.D., S.X., M.S., X.C., and S.L. discussed the results and edited the paper.

Data Availability Statement
The data that support the findings of this study are available from the corresponding authors upon reasonable request.

Received: ((will be filled in by the editorial staff))
Revised: ((will be filled in by the editorial staff))
Published online: ((will be filled in by the editorial staff))

References

[1] P. Simon, Y. Gogotsi, B. Dunn, *Science* **2014**, *343*, 1210.

[2] P. Simon, Y. Gogotsi, *Nat. Mater.* **2008**, *7*, 845.

[3] a) J. Chmiola, G. Yushin, Y. Gogotsi, C. Portet, P. Simon, P. L. Taberna, *Science* **2006**, *313*, 1760; b) H. Shao, Y. C. Wu, Z. Lin, P. L. Taberna, P. Simon, *Chem. Soc. Rev.* **2020**, *49*, 3005.

[4] a) J. Huang, B. G. Sumpter, V. Meunier, *Angew. Chem. Int. Ed.* **2008**, *47*, 520; b) C. Merlet, B. Rotenberg, P. A. Madden, P. L. Taberna, P. Simon, Y. Gogotsi, M. Salanne, *Nat. Mater.* **2012**, *11*, 306.

[5] a) S. Kondrat, N. Georgi, M. V. Fedorov, A. A. Kornyshev, *Phys. Chem. Chem. Phys.* **2011**, *13*, 11359; b) C. Merlet, C. Péan, B. Rotenberg, P. A. Madden, B. Daffos, P.-L. Taberna, P. Simon, M. Salanne, *Nat. Commun.* **2013**, *4*, 2701.

[6] a) M. Salanne, B. Rotenberg, K. Naoi, K. Kaneko, P.-L. Taberna, C. P. Grey, B. Dunn, P. Simon, *Nat. Energy* **2016**, *1*, 16070; b) M. D. Levi, N. Levy, S. Sigalov, G. Salitra, D. Aurbach, J. Maier, *J. Am Chem. Soc.* **2010**, *132*, 13220; c) H. Wang, A. C. Forse, J. M. Griffin, N. M. Trease, L. Trognko, P.-L. Taberna, P. Simon, C. P. Grey, *J. Am. Chem. Soc*. **2013**, *135*, 18968; d) W.-Y. Tsai, P.-L. Taberna, P. Simon, *J. Am. Chem. Soc*. **2014**, *136*, 8722; e) A. C. Forse, J. M. Griffin, C. Merlet, J. Carretero-Gonzalez, A.-R. O. Raji, N. M. Trease, C. P. Grey, *Nat. Energy* **2017**, *2*, 16216; f) C. Prehal, C. Koczwara, N. Jäckel, A. Schreiber, M. Burian, H. Amenitsch, M. A. Hartmann, V. Presser, O. Paris, *Nat. Energy* **2017**, *2*, 16215; g) J. M. Griffin, A. C. Forse, W.-Y. Tsai, P.-L. Taberna, P. Simon, C. P. Grey, *Nat. Mater.* **2015**, *14*, 812; h) C. Prehal, D. Weingarth, E. Perre, R. T. Lechner, H. Amenitsch, O. Paris, V. Presser, *Energy Environ. Sci.* **2015**, *8*, 1725; i) R. Futamura, T. Iiyama, Y. Takasaki, Y. Gogotsi, M. J. Biggs, M. Salanne, J. Ségalini, P. Simon, K. Kaneko, *Nat. Mater.* **2017**, *16*, 1225; j) M. Deschamps, E. Gilbert, P. Azais, E. Raymundo-Piñero, M. R. Ammar, P. Simon, D. Massiot, F. Béguin, *Nat. Mater*. **2013**, *12*, 351; k) A. C. Forse, J. M. Griffin, C. Merlet, P. M. Bayley, H. Wang, P. Simon, C. P. Grey, *J. Am. Chem. Soc.* **2015**, *137*, 7231; l) A. J. Ilott, N. M. Trease, C. P. Grey, A. Jerschow, *Nat. Commun.* **2014**, *5*, 4536.

[7] a) M. Newville, *Rev. Mineral. Geochem.* **2014**, *78*, 33; b) Y. Du, Y. Zhu, S. Xi, P. Yang, H. O. Moser, M. B. H. Breese, A. Borgna, *J. Synchrotron Radiat.* **2015**, *22*, 839; c) Y. Tang, Y. Zhang, O. I. Malyi, N. Bucher, H. Xia, S. Xi, Z. Zhu, Z. Lv, W. Li, J. Wei, M. Srinivasan, A. Borgna, M. Antonietti, Y. Du, X. Chen, *Adv. Mater.* **2018**, *30*, 1802200.

[8] a) T. Ohkubo, T. Konishi, Y. Hattori, H. Kanoh, T. Fujikawa, K. Kaneko, *J. Am. Chem. Soc.* **2002**, *124*, 11860; b) P. D'Angelo, M. Benfatto, S. D. Longa, N. V. Pavel, *Phys. Rev. B* **2002**, *66*, 064209.

[9] a) T. Ling, P. Da, X. Zheng, B. Ge, Z. Hu, M. Wu, X. W. Du, W. B. Hu, M. Jaroniec, S. Z. Qiao, *Sci. Adv.* **2018**, *4*, eaau6261; b) H. Ma, H. Chen, M. Wu, F. Chi, F. Liu, J. Bai, H. Cheng, C. Li, L. Qu, *Angew. Chem. Int. Ed.* **2020**, *59*, 14541; c) Z. Huang, T. Wang, H. Song, X. Li, G. Liang, D. Wang, Q. Yang, Z. Chen, L. Ma, Z. Liu, B. Gao, J. Fan, C. Zhi, *Angew. Chem. Int. Ed.* **2021**, *60*, 1011.

[10] D. Chao, W. Zhou, F. Xie, C. Ye, H. Li, M. Jaroniec, S. Z. Qiao, *Sci. Adv.* **2020**, *6*, eaba4098.

[11] a) S. Porada, R. Zhao, A. van der Wal, V. Presser, P. M. Biesheuvel, *Prog. Mater. Sci.* **2013**, *58*, 1388; b) G. Harper, R. Sommerville, E. Kendrick, L. Driscoll, P. Slater, R. Stolkin, A. Walton, P. Christensen, O. Heidrich, S. Lambert, A. Abbott, K. Ryder, L. Gaines, P. Anderson, *Nature* **2019**, *575*, 75.

[12] J. W. Smith, R. J. Saykally, *Chem. Rev.* **2017**, *117*, 13909.

[13] a) T. Yamamoto, *X-ray Spectrom.* **2008**, *37*, 572; b) K. Saravanan, A. Jarry, R. Kostecki, G. Chen, *Sci. Rep.* **2015**, *5*, 8027.

[14] a) Y. Tian, B. Estschmann, W. Liu, S. Borg, Y. Mei, D. Testemale, B. O'Neill, N. Rae, D. M. Sherman, Y. Ngothai, B. Johannessen, C. Glover, J. Brugger, *Chem. Geol.* **2012**, *334*, 345; b) A. van der Ent, D. L. Callahan, B. N. Noller, J. Mesjasz-Przybylowicz, W. J. Przybylowicz, A. Barnabas, H. H. Harris, *Sci. Rep.* **2017**, *7*, 41861.

[15] a) M. Ocaña, *Colloid Polym. Sci.* **2000**, *278*, 443; b) G. Defontaine, L. J. Michot, I. Bihannic, J. Ghanbaja, V. Briois, *Langmuir* **2003**, *19*, 10588; c) T. Ling, M. Jaroniec, S.-Z. Qiao, *Adv. Mater.* **2020**, *32*, e2001866.

[16] Y. Ye, J. E. Thorne, C. H. Wu, Y.-S. Liu, C. Du, J.-W. Jang, E. Liu, D. Wang, J. Guo, *J. Phys. Chem. B* **2018**, *122*, 927.

[17] M. Antonietti, X. Chen, R. Yan, M. Oschatz, *Energy Environ. Sci.* **2018**, *11*, 3069.

[18] L. A. Belfiore, H. Graham, E. Ueda, *Macromolecules* **1992**, *25*, 2935.

[19] H. Kim, G. Yoon, I. Park, K.-Y. Park, B. Lee, J. Kim, Y.-U. Park, S.-K. Jung, H.-D. Lim, D. Ahn, S. Lee, K. Kang, *Energy Environ. Sci.* **2015**, *8*, 3325.

[20] a) R. N. Collins, K. M. Rosso, A. L. Rose, C. J. Glover, T. D. Waite, *Geochim. Cosmochim. Acta* **2016**, *177*, 150; b) M. K. Doula, A. Ioannou, *Microporous and Mesoporous Mater.* **2003**, *58*, 115; c) J. W. Lee, J. M. Ko, J.-D. Kim, *J. Phys. Chem. C* **2011**, *115*, 19445.

[21] D. Aurbach, M. D. Levi, G. Salitra, N. Levy, E. Pollak, J. Muthu, *J. Electrochem. Soc.* **2008**, *155*, A745.

[22] a) K. Cao, J. Biskupek, C. T. Stoppiello, R. L. McSweeney, T. W. Chamberlain, Z. Liu, K. Suenaga, S. T. Skowron, E. Besley, A. N. Khlobystov, U. Kaiser, *Nat. Chem.* **2020**, *12*, 921; b) S. Jeon, T. Heo, S. Y. Hwang, J. Ciston, K. C. Bustillo, B. W. Reed, J. Ham, S. Kang, S. Kim, J. Lim, K. Lim, J. S. Kim, M. H. Kang, R. S. Bloom, S. Hong, K. Kim, A. Zettl, W. Y. Kim, P. Ercius, J. Park, W. C. Lee, *Science* **2021**, *371*, 498.

[23] J. Chmiola, C. Largeot, P. L. Taberna, P. Simon, Y. Gogotsi, *Angew. Chem. Int. Ed.* **2008**, *47*, 3392.

[24] L.-Q. Mai, A. Minhas-Khan, X. Tian, K. M. Hercule, Y.-L. Zhao, X. Lin, X. Xu, *Nat. Commun.* **2013**, *4*, 2923.

[25] B. Ravel, M. Newville, *J. Synchrotron Radiat.* **2005**, *12*, 537.

[26] X. J. Yu, C. Z. Diao, T. Venkatesan, M. B. H. Breese, A. Rusydi, *Rev. Sci. Instrum.* **2018**, *89*, 113113.

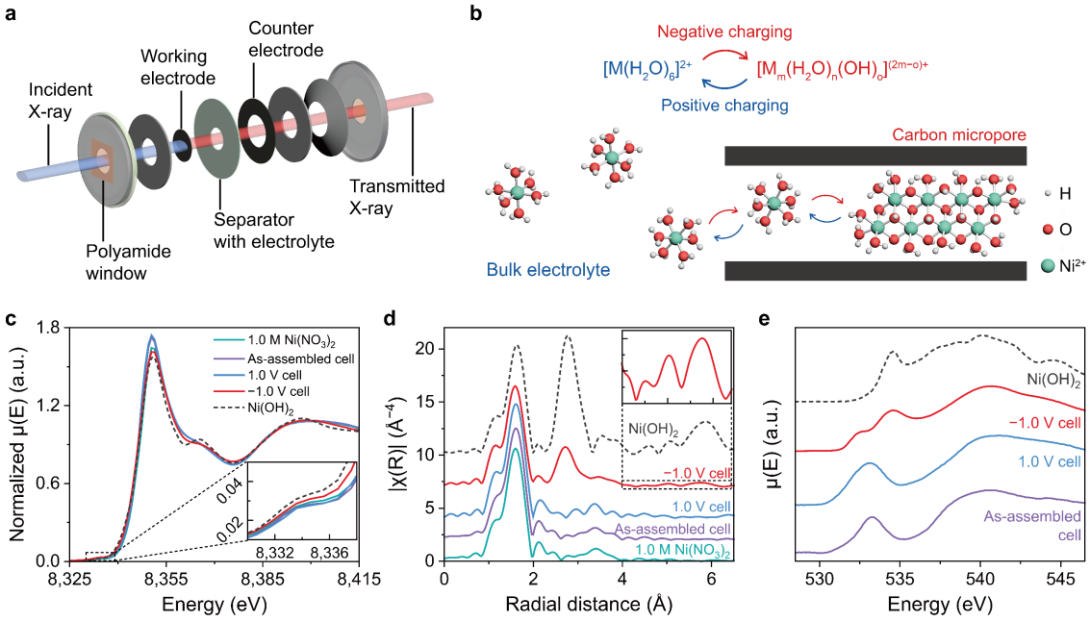

Figure 1. Structural anomalies of Ni aqua ions inside negatively charged carbon micropores. a) Scheme of the customized coin cell with polyamide windows and disk–ring electrode configuration for in situ XAS measurements. The X-ray only penetrates the working electrode during measurements. b) Scheme of the reversible oligomerization of transition metal aqua ions during charging of a carbon micropore, with Ni aqua ion as the example. c) Ni K edge normalized XANES spectra of 1.0 M $Ni(NO_3)_2$ aqueous electrolyte, as-assembled cell, cells at ±1.0 V, and $Ni(OH)_2$. The turquoise, purple, and blue curves are overlapping. Inset: zoomed pre-edge features. d) EXAFS |χ(R)| spectra of the samples. Inset: zoomed features of the red curve in 4–6.5 Å. The new peaks in −1.0 V cell spectrum resemble the peaks in $Ni(OH)_2$ spectrum. e) O K edge XAS spectra of the samples. The dual peaks of the −1.0 V cell between 530–535 eV meet the peaks of the as-assembled cell and $Ni(OH)_2$.

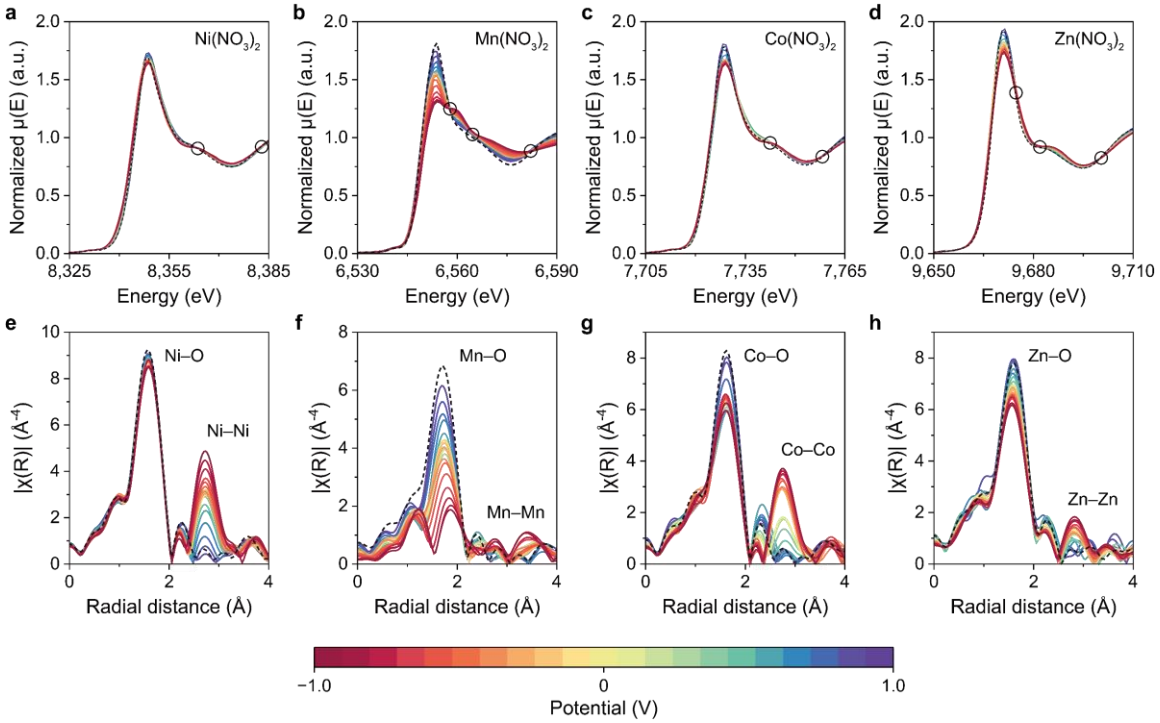

Figure 2. Reversible oligomerization of transition metal aqua ions during chronoamperometry charging. a–d) Operando transition metal K edge normalized XANES spectra of the customized microporous carbon cells during chronoamperometry charging between 0 to ±1.0 V with 1.0 M (a) $Ni(NO_3)_2$, (b) $Mn(NO_3)_2$, (c) $Co(NO_3)_2$, and (d) $Zn(NO_3)_2$ electrolytes. The dash curves represent the spectra of the electrolytes. The circuits highlight the isosbestic points. e–h) The corresponding EXAFS $|\chi(R)|$ spectra of the cells. The dash curves represent the spectra of the electrolytes. All the cations associate into ionic oligomers with the raising of M–M scattering peaks upon negative charging, as well as dissociate with the M–M peaks dropping during positive charging. The drop in M–O peaks for Mn, Co, and Zn aqua ions indicates partial desolvation of the octahedrally solvated ions, while Ni aqua ions retain octahedral geometry.

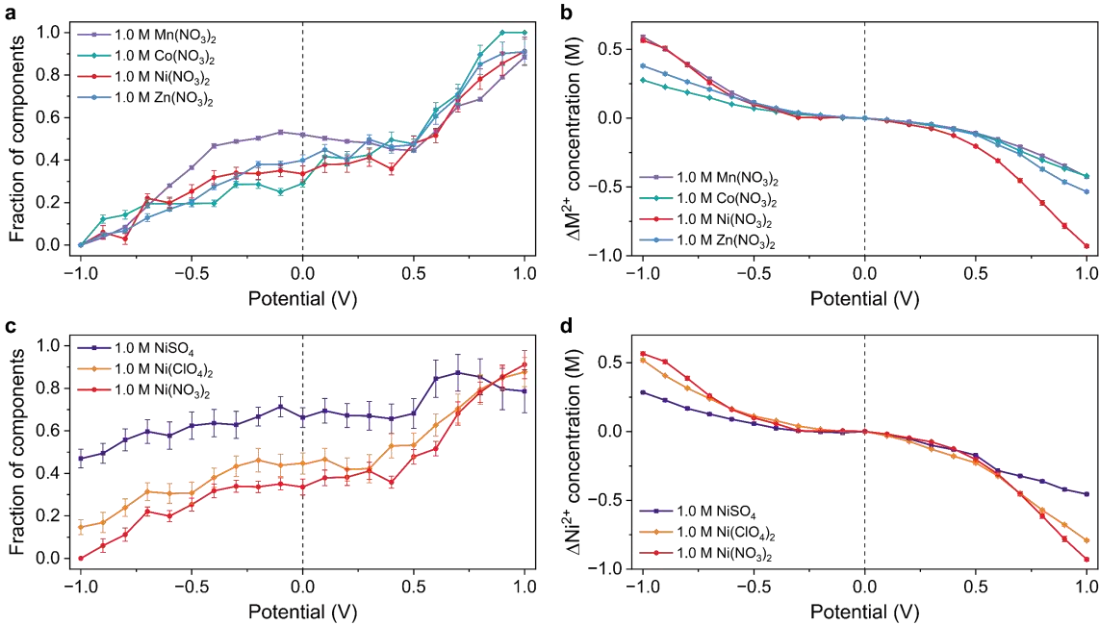

Figure 3. Quantification of the ion-specific oligomerization and migration processes. a) LCF fitted compositions of transition metal ions in the working electrode of cells during chronoamperometry charging, using the spectra of electrolytes and cells at −1.0 V state as the end members representing 1 (solvated ions) and 0 (ionic oligomers), respectively. b) Corresponding concentration changes calculated from the edge step of the spectra. c) LCF fitted compositions of Ni ions in the working electrode of cells during chronoamperometry charging coupled with different anions, using the spectra of 1.0 M $Ni(NO_3)_2$ and $Ni(NO_3)_2$ cell at −1.0 V as the LCF end members representing 1 (solvated ion) and 0 (ionic oligomer), respectively. d) Corresponding concentration changes calculated from the edge step of the spectra. Error bars in (a) and (c) represent the uncertainty from LCF. Error bars in (b) and (d) represent the standard deviations of the mean concentration values from three independent XAS measurements, which are very small and almost invisible.

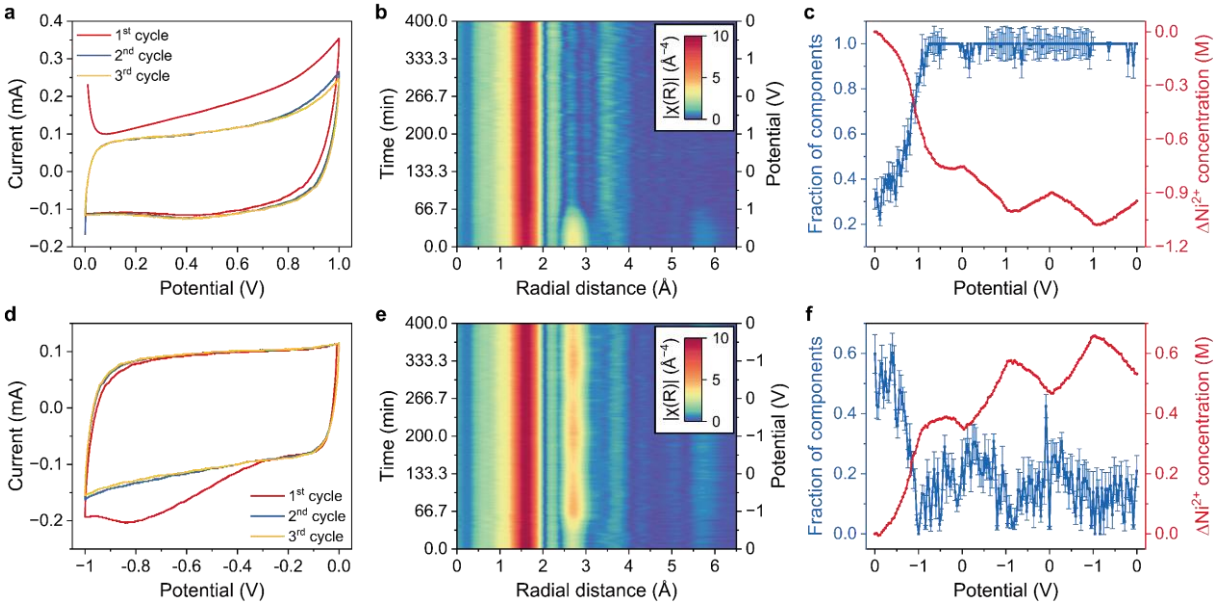

Figure 4. Continuous monitoring of the oligomerization and migration of Ni aqua ions. a, d) CV curves of the customized microporous carbon cells at 0.25 mV s^{-1} scan rate between (a) 0 to 1.0 V and (d) 0 to −1.0 V. The rectangular curve indicates typical capacitive energy storage characteristic, while the first charging curves diverge from the rest and represent more energy consumption due to the activation processes, etc.[21] b, e) Successive 2D contour plots of the operando EXAFS |χ(R)| spectra during (b) positive and (e) negative CV cycles. The Ni–Ni scattering peak at 2.73 Å fades during first positive charging and oscillates up and down during negative cycling, while the Ni–O scattering peak at 1.61 Å remains stable. c, f) Composition (blue) and concentration (red) changes of Ni ions in the working electrode of cells during the (c) positive and (f) negative CV cycles. The spectra of the ±1.0 V states are used as the LCF end members representing 1 (1.0 V, solvated ion) and 0 (−1.0 V, ionic oligomer). Error bars represent the uncertainty from LCF (blue).

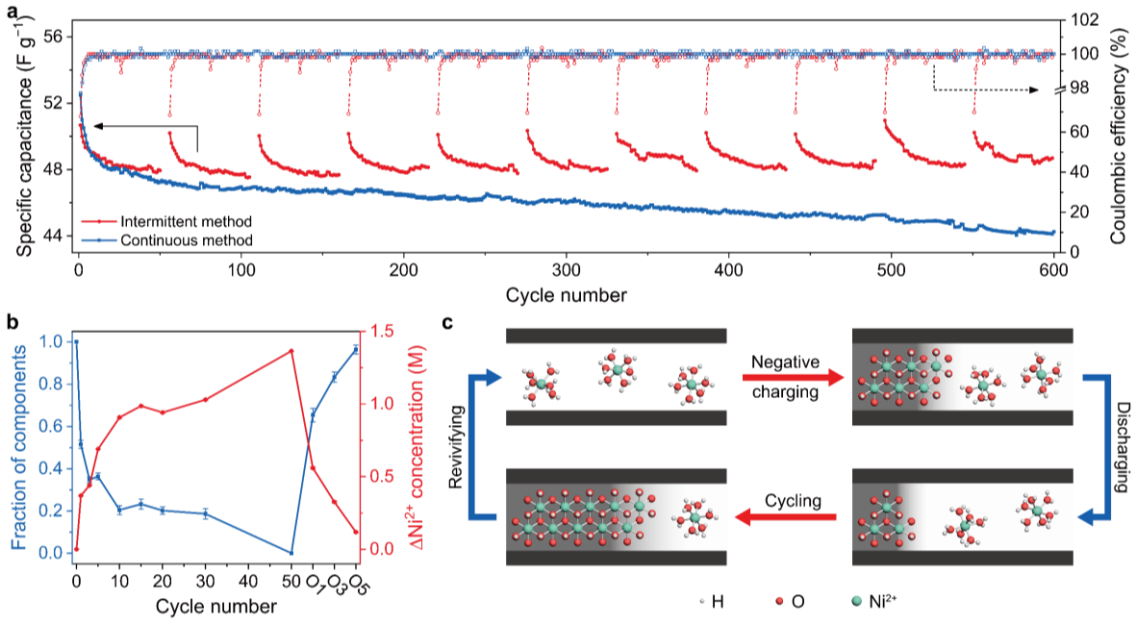

Figure 5. Capacitance fading and revivification of carbon micropores. a) Specific capacitance of customized microporous carbon cells with 1.0 M $Ni(NO_3)_2$ electrolyte cycling between 0 to −1.0 V. Continuous cycling (blue) as well as intermittent cycling with 5 opposite cycles between every 50 cycles (red) are used. The latter keeps more capacitance than the former. b) Composition (blue) and concentration (red) changes of Ni ions in the working electrode of cells after different cycles. O1, O3, and O5 represent the 1st, 3rd, and 5th opposite cycles. The spectra of the as-assembled cell and cell after 50 cycles are used as the LCF end members representing 1 (solvated ion) and 0 (ionic oligomer). Error bars represent the uncertainty from LCF (blue) and the standard deviation of the mean concentration value from three independent measurements (red). The changes in charge storage and XAS spectra together prove that the accumulation of ionic oligomers causes capacitance fading of the supercapacitor. c) Scheme of the ionic oligomer accumulation inside a carbon micropore. Oligomers form during negative charging but are not fully destructed during discharging due to the sluggish dissociation kinetics. As a result, they accumulate with cycling and block the micropore (deeper background color) from further charge storage.

Oligomerization of transition metal aqua ions inside electrified carbon micropores is observed using in situ X-ray absorption spectroscopy. The cations associate together via hydroxo bridging under the synergy of confinement and negative charging. The resulted ionic oligomers have sluggish dissociation kinetics and accumulate upon cycling, leading to capacitance fading of supercapacitors. Positive charging destructs them and revivifies the capaictance.

Jiaqi Wei, Lixiang Zhong, Huarong Xia, Zhisheng Lv, Caozheng Diao, Wei Zhang, Xing Li, Yonghua Du, Shibo Xi,* Mathieu Salanne,* Xiaodong Chen,* and Shuzhou Li*

Metal Ion Oligomerization inside Electrified Carbon Micropores and Its Effect on Capacitive Charge Storage

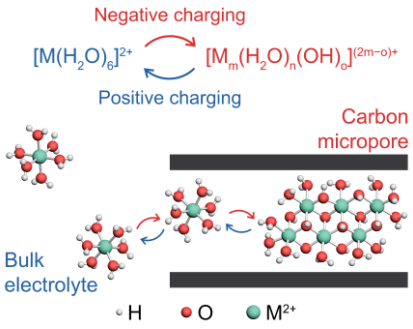

Supporting Information

Metal Ion Oligomerization inside Electrified Carbon Micropores and Its Effect on Capacitive Charge Storage

Jiaqi Wei, Lixiang Zhong, Huarong Xia, Zhisheng Lv, Caozheng Diao, Wei Zhang, Xing Li, Yonghua Du, Shibo Xi, Mathieu Salanne,* Xiaodong Chen,* and Shuzhou Li**

Table of Contents

1. Supporting Notes

1.1 DFT Calculations and FDMNES XAS Simulations: Spin-polarized DFT calculations as implemented in the Vienna ab initio simulation package were performed using the plane-wave pseudopotential basis set to optimize the tetrahedrally solvated Mn, Co, and Zn ionic oligomer structures.[1] The ion–electron interactions were treated with the projected augmented wave pseudopotentials,[2] and the generalized gradient approximation parametrized by Perdew, Burke, and Ernzerh was used to describe the electronic exchange-correlation energy.[3] Effective Hubbard parameters of 5.25, 4.00, and 0 eV were added for the Mn, Co, and Zn 3d states. The cut-off energy for plane-wave expansion was set to 400 eV. All structures were relaxed by the conjugate gradient method until the force component on each atom was less than 0.01 eV $Å^{-1}$. The convergence criteria of total energy in the self-consistent field method was set to 10^{-5} eV.

Mn, Co, and Zn K edge theoretical XAS spectra of the DFT optimized structures were simulated using the finite difference method (FDM), which was implemented within the Finite Difference Method Near Edge Scattering (FDMNES) package developed by Joly.[4] A free form self-consistent field (SCF) potential of radius 6.0 Å around the absorbing atoms was used. Broadening contributions from the core–hole lifetime, the inelastic plasmon interaction with photoelectron, the resolution of the beamline, and the Fermi energy were accounted for using an arctangent convolution.[5]

1.2 Calculation of Ion Concentration with XAS Edge Step: XAS measures the X-ray absorption coefficient (μ) of specific elements, which can be analyzed to get the electron configuration and local geometry, etc. of the targeting element. For transmission mode XAS, $\mu(E)$ is determined by the ratio of the transmitted X-ray (I_t) and incident X-ray (I_0) via the following equation:

$$\mu(E) = -\ln\frac{I_t}{I_0} \quad (1)$$

For chemical compounds and mixtures, μ(E) of a specific element can be identified from total μ(E) at and above its X-ray absorption edge energy due to its greatly increased absorption with relatively constant absorption of other elements (Figure S8). In general, the intensity of an XAS spectrum is positively correlated to the attenuation mass along the X-ray transmission path, since more matter results in heavier X-ray attenuation and thus smaller I_t. As a result, the population of target elements can be estimated from their XAS spectra intensity. For transition metal K edge XAS, the intensity of μ(E) is evaluated by its edge step, which is extrapolated as the difference between post-edge and pre-edge line at the reference energy (E_0, the energy of the first peak in the first derivative of μ(E)) and is linearly correlated to the quantity of the transition metal element. For Mn, Co, Ni, and Zn, an edge step of 1.0 is estimated to be 0.03444, 0.04027, 0.05868, and 0.05236 mmol atoms, respectively, in a 1.0 cm diameter disk, based on the set-up of XAFCA beamline. As such, their concentration (M) can be calculated by the following equation:

$$C_M = {edge\ step \times molar\ factor}/{t \times \pi \times 0.5^2} \quad (2)$$

where C (M) is the ion concentration and t (cm) is the average sample thickness.

In this work, the XAS signal comes from the transition metal aqua ions in the electrolytes adsorbed by the porous carbon electrode. The sample thickness is therefore the electrolyte thickness, which can be calculated from Equation S2 with the μ(E) edge step of the as-assembled cell, assuming a thorough infiltration and a uniform 1.0 M concentration of the electrolyte in the as-assembled electrode. The electrolyte thickness was calculated to be around 30.99, 33.68, 36.35, and 33.59 μm per mg of the electrode for Mn, Co, Ni, and Zn aqua ions, respectively (Figure S8). These estimated thicknesses lead to around 30% more electrolyte volume than the pore volume of the activated carbon measured by N_2 sorption experiment

(Figure S1 and Table S1), which is ascribed to the electrolyte in the vicinity of carbon particles and on the outer electrode surface, etc. (Figure S8). Further calculations of the ion concentration were done with Equation S2 based on these thickness and individual edge step of each XAS spectrum.

It should be noticed that the calculated ion concentration corresponds to, instead of electrolyte inside carbon micropores, the entire electrolyte volume along the X-ray transmission path (in all pore size regimes, in vicinities between carbon particles, and on the electrode surface) and thus should be deviated slightly from the actual ion concentration inside carbon micropores. Nevertheless, considering the large portion of carbon micropores, this result should be meaningful in examining ion migration on the working electrode during the operation of supercapacitors.

1.3 EXAFS Fitting of Ni K Edge XAS: The EXAFS of an atom arises mainly from single scattering of the photoelectron from neighbors, which can continue for 1000 eV after XANES and tells the local chemical geometry and coordination details, etc. of the target atom. In general, contributions to the EXAFS oscillation from scatterings of different neighboring atoms can be described by the following EXAFS equation:

$$\chi(k) = \sum_j \frac{{S_0}^2 N_j f_j(k) e^{-2R_j/\lambda(k)} e^{-2k^2{\sigma_j}^2}}{k{R_j}^2} \sin\left[2kR_j + \delta_j(k)\right] \quad (3)$$

where *j* represents the individual coordination of identical atoms at a similar distance from the target, *f(k)* and *δ(k)* are scattering amplitude and phase-shift of the atoms, S_0^2 is the amplitude reduction factor, *N* is the coordination number, *R* is the coordination distance, and σ^2 is the disorder. With this equation, the coordination number, distance, and disorder can be evaluated by fitting the EXAFS spectra.

In this work, EXAFS fitting was applied to the Ni K edge |χ(R)| spectra using the Artemis software with EFFF6 code.[6] The fitting k-range was set to be 2.5–12.5 with k-weight of 1, 2 and 3. The fitting r-range was set to be 1.0–3.3. Ni–O and Ni–Ni scattering paths extracted from $Ni(OH)_2$ structure were fitted. Four fitting parameters were extracted from the EXAFS equation, which are: the coordination number *N*, the Debye-Waller factor σ^2 for the mean-square relative displacement of the structure (thermal and structural disorder), the energy shift ΔE_0 to correct the discrepancy between standard E_0 and calculation, and the coordination distance *R* from center Ni^{2+} to neighboring atoms. Considering the almost unchanged XANES spectra and Ni–O scattering peaks, the Ni–H_2O/OH^- coordination are treated as one scattering path. This leads to 8 fitting parameters in total. The scattering numbers of Ni–O and Ni–Ni are normalized with the S_0^2 of the fitting result of $Ni(OH)_2$ spectrum (0.803 for Ni–O and 0.924 for Ni–Ni).

1.4 Isosbestic Point and Linear Combination Fitting of XAS: For a sample with different phases or components of the same elements, the μ(E) of each phase or component is usually different from each other, leading to distinct X-ray absorption and various total XAS spectrum. For a two-phase transformation, the total X-ray absorption of the sample can be expressed as:

$$Absorption = T(\alpha_A c_A + \alpha_B c_B) \quad (4)$$

where T is the sample thickness, α is the absorption coefficient, and c is the concentration.

At certain energies, the μ(E) of two phases or components could be the same ($\alpha_A = \alpha_B$). For systems with constant thickness T and total concentration ($c_A + c_B$), the same μ(E) give rise to composition-independent total X-ray absorption, exhibiting as crossing points in the spectrum called isosbestic point, which is the specific point of energy or frequency at which μ(E) of the sample is constant regardless of the extent of chemical reactions or phase transformations. For systems with two-phase transformation but varying total concentration, isosbestic points can still be observed in the normalized μ(E) spectra, which rules out the influence of sample amount to the overall spectra but leaves the influence of the ratio of two phases.

For systems with two-phase transformation, their XAS spectra during the transformation with unknown phase ratio can be fitted in the form of normalized μ(E), derivative μ(E), or χ(k) with the standard spectra at the two ends of the transformation, which is known as LCF. By fitting the intermediate spectra as linear combinations of the end members, the rate of the transformation and the composition of the samples can be quantitatively deduced.

In this work, the operando transition metal K edge XAS normalized μ(E) spectra were fitted with LCF in the energy range around 6530–6650 eV for Mn, 7700–7820 eV for Co, 8320–8440 eV for Ni, and 9645–9765 eV for Zn, respectively.

2. Supporting Figures and Tables

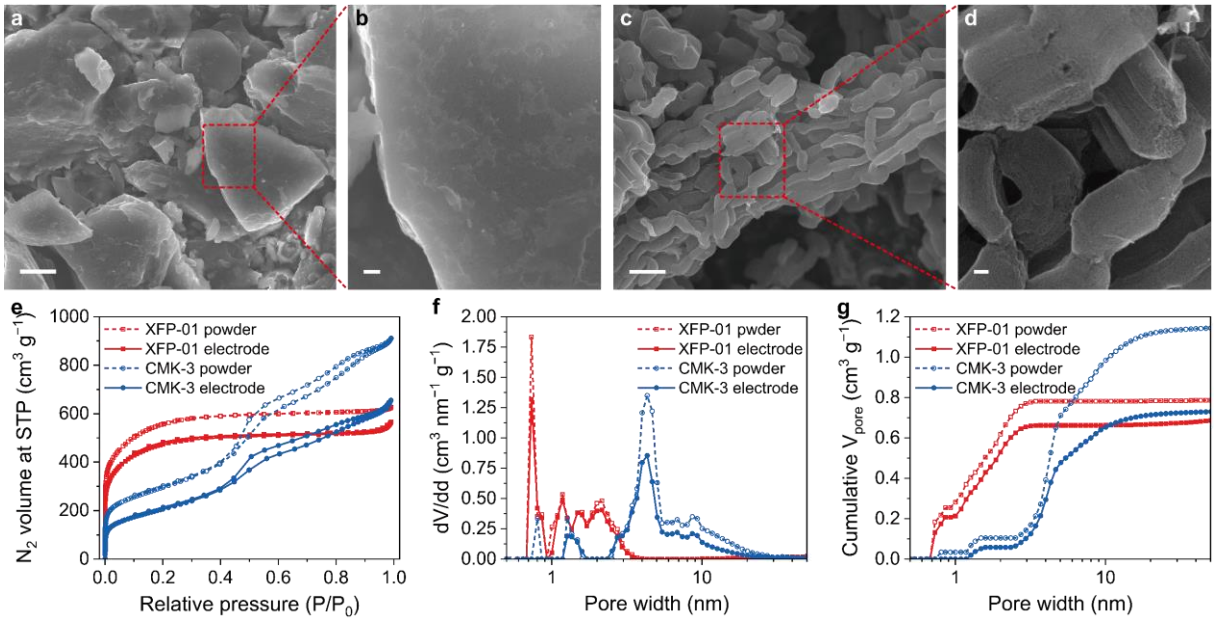

Figure S1. Characterizations of the carbon materials. a–d) Morphology of (a), (b) XFP-01 and (c), (d) CMK-3. The scale bars in (a) and (c) represent 1 μm, while the scale bars in (b) and (d) represent 100 nm. e–g) Porosity analysis of the carbons and their electrodes with (e) N_2 sorption isotherms, as well as (f) pore size distribution and (g) cumulated pore volume calculated by the original DFT model.

Figure S1 shows the morphology and porosity of the carbons and their electrodes. XFP-01 is nano/micro-particle, while CMK-3 shows wormhole structure with oriented tubular channels. N_2 sorption isotherms of XFP-01 and its electrode have type I features based on IUPAC classification.[7] The higher N_2 adsorption at $P/P_0 < 0.2$ indicates the presence of micropores and small mesopores. On the other hand, isotherms of CMK-3 and its electrode are type IV with hysteresis loop and higher N_2 uptake at $P/P_0 > 0.4$, which represent a macropore/mesopore-rich structure. XFP-01 and its electrode have pore sizes between 0.5–3.0 nm, concentrated at 0.75 nm, while CMK-3 and its electrode show pore size concentrated at 4.5 nm. The specific surface area and pore volume reduce slightly for the electrodes compared to the carbons, which is due to the binder blocking some of the pores. The comparable pore size to transition metal aqua ions guarantees XFP-01 as an ideal platform to study the structure of the cations under spatial confinement,[8] while CMK-3 is a good control group with minimal carbon micropores. The key structural parameters are summarized in Table S1.

Table S1. N_2 sorption analysis results for the carbons and their electrodes.

Sample	Specific surface area ($m^2\ g^{-1}$)		Micropore volume ($cm^3\ g^{-1}$)	Nonmicropore volume ($cm^3\ g^{-1}$)	$V_{micro}/V_{nonmicro}$
	BET	Original DFT			
XFP-01	1880.3	1333.6	0.618	0.173	3.57
XFP-01 electrode	1602.4	1115.7	0.530	0.187	2.83
CMK-3	1051.0	624.2	0.104	1.047	0.10
CMK-3 electrode	749.9	420.7	0.058	0.680	0.09

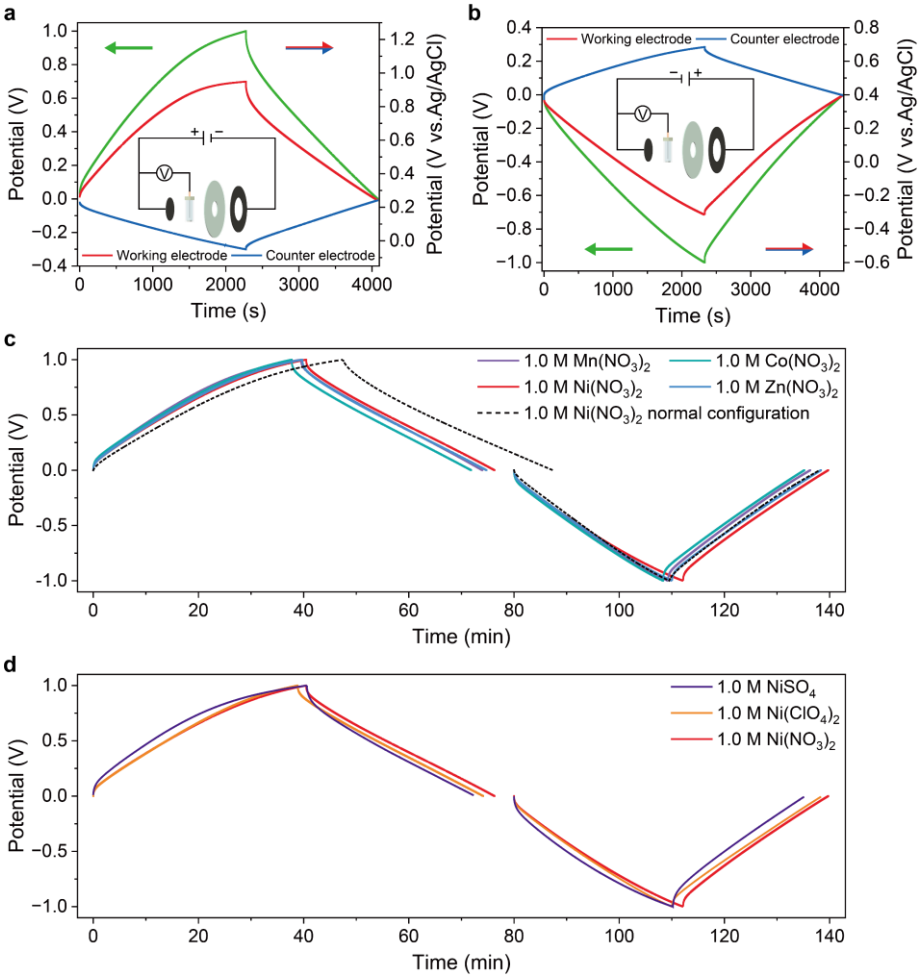

Figure S2. Capacitive energy storage performance of the customized microporous carbon cells. a, b) Potential distributions on the microporous carbon working and counter electrodes during (a) positive and (b) negative charging/discharging with 1.0 M $Ni(NO_3)_2$ electrolyte. Inset: scheme of the testing circuit for analyzing the potential distributions with Ag/AgCl reference. c, d) Charging/discharging curves of the customized microporous carbon cells using 1.0 M (c) nitrate electrolytes with varying cations and (d) Ni^{2+} electrolytes with varying anions.

The capacitive energy storage performance of the customized coin cell was tested with microporous carbon electrodes and various transition metal ion aqueous electrolytes. As shown in Figure S2, the potential distribution is uneven because of the unequal mass of the working and counter electrode,[9] which leads to more potential on the smaller working electrode and thus larger potential window for ion behavior studies. Electrolytes with varying cations or anions show similar energy storage behaviors for both positive and negative charging/discharging, which are also very similar to cell with the same mass ratio but commercial configuration. This guarantees the customized cell as an ideal platform for operando analysis of ion behaviors under real electrochemical test conditions.

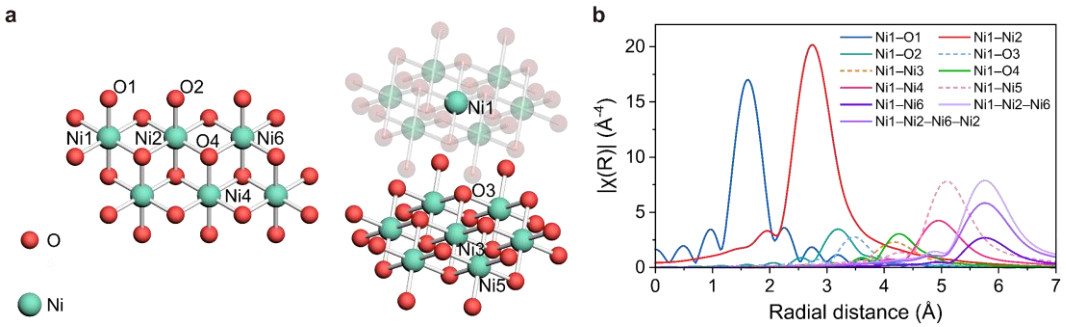

Figure S3. Structural origin of $Ni(OH)_2$ EXAFS signals. a) Scheme of $Ni(OH)_2$ structures within one layer (left) and between layers (right). Notations Ni1 represents the centering Ni^{2+}, while the rest notations represent different coordination shells around Ni1 with strong EXAFS responses, numbered with increasing distances. The hydrogen atoms are hidden in the structures for a clearer view. b) Theoretical EXAFS $|\chi(R)|$ peaks of the coordination shells around Ni1. The solid curves represents coordinations within the same $Ni(OH)_2$ layer, while the dash curves represent coordinations from adjacent layers.

The origin of scattering peaks in the experimental $|\chi(R)|$ spectra, which resemble the peaks of $Ni(OH)_2$ (Figure 1d), is analyzed by matching to the structure and theoretical $|\chi(R)|$ spectrum of $Ni(OH)_2$. As shown in Figure S3, $Ni(OH)_2$ has layered structure of Ni^{2+} that are octahedrally coordinated to hydroxide groups, while each hydroxide group is linked to 3 Ni^{2+}, serving as the bridge connecting Ni^{2+}. Multiple layers of such structure stuck together, forming $Ni(OH)_2$. Taking Ni1 as the X-ray absorbing atom, Ni2–Ni5 and O1–O4 mark the significant coordinations surround it. With this structure, theoretical $|\chi(R)|$ peaks of the significant scattering paths were generated using the Artemis software.[6] The peaks show good agreement with the experimental $|\chi(R)|$ spectrum of the −1.0 V cell, especially for the newly arisen peaks at 2.73 Å, 5.02 Å, and 5.78 Å. Therefore, the newly arisen peaks in the −1.0 V cell spectrum are ascribed to Ni–Ni coordinations with $Ni(OH)_2$-like structure, which arise from the order packing of Ni aqua ions with hydroxo bridging inside negatively charged micropores.

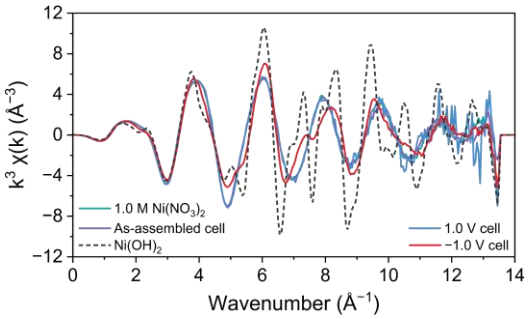

Figure S4. EXAFS analysis of the samples in k-space. Ni K edge $k^3\chi(k)$ spectra for 1.0 M $Ni(NO_3)_2$ aqueous electrolyte, as-assembled cell, cells at ±1.0 V, and $Ni(OH)_2$.

Apart from normalized μ(E) and |χ(R)|, clear derivation of −1.0 V cell spectrum from the rest samples was also observed in the EXAFS $k^3\chi(k)$ spectra: the trough around 4.9 $Å^{-1}$ becomes shallower with a small new crest around 5.2 $Å^{-1}$ formed; the crest at 6.1 $Å^{-1}$ raises; the trough at 7.0 $Å^{-1}$ is left-shifted; the raising waist at 7.4 $Å^{-1}$ splits into one crest and one trough; etc. These spectral changes resemble the spectra of $Ni(OH)_2$, which further confirms the formation of $Ni(OH)_2$-like structure in the −1.0 V cell.

a

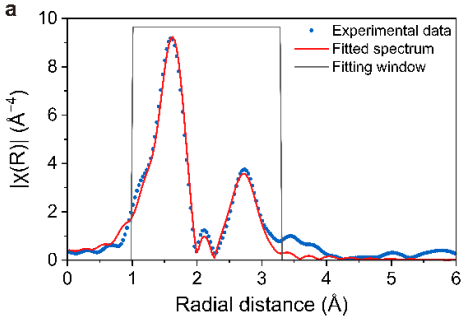

b

Fitting path	Ni–O	Ni–Ni
Coordination number	6.22±0.43	3.52±1.42
Coordination distance (Å)	2.05±0.01	3.10±0.03
ΔE_0 (eV)	−1.73±0.79	−1.12±3.11
Debye–Waller factor (10^{-3} Å^2)	6.95±1.28	12.13±4.14
R-factor	0.008	

Figure S5. Quantification of the $Ni(OH)_2$-like coordination. a) Experimental (blue dots) and fitted (red curve) $|\chi(R)|$ spectrum of the −1.0 V cell. The spectra align very well in the fitting r-range of 1.0–3.3. b) Fitting results of the −1.0 V cell spectrum. The coordination numbers of Ni–O and Ni–Ni paths are normalized with the amplitude reduction factor of $Ni(OH)_2$ spectrum.

To quantify the coordination information of Ni^{2+} in the −1.0 V cell, EXAFS fitting was applied to the $|\chi(R)|$ spectra using the Artemis software with $Ni(OH)_2$ structure as the fitting model.[6] As shown in Figure S5, the fitted curve overlaps perfectly with the experimental result with an R-factor of only 0.008, indicating an ideal and reliable fitting. The fitted Ni–O peak shows coordination number of 6.22 and distance around 2.05 Å, which agree with both $[Ni(H_2O)_6]^{2+}$ and $Ni(OH)_2$. The Ni–Ni peak has fitted coordination number of 3.52 and distance around 3.10 Å. While the coordination distance meets the one for $Ni(OH)_2$ well, the smaller average coordination number than $Ni(OH)_2$ indicates the formation of small ionic oligomers with large amount of edge and corner Ni^{2+}, which have unsaturated Ni–Ni coordination. Based on the structure of $Ni(OH)_2$, an average coordination number of 3.52 suggests more than 8 Ni^{2+} in an average oligomer considering the most effective connecting method and the solvated ion–oligomer mixing nature of the XAS signal. This might be interesting for catalytical applications considering the high catalytic activity of such small $Ni(OH)_2$ nanomaterials.[10]

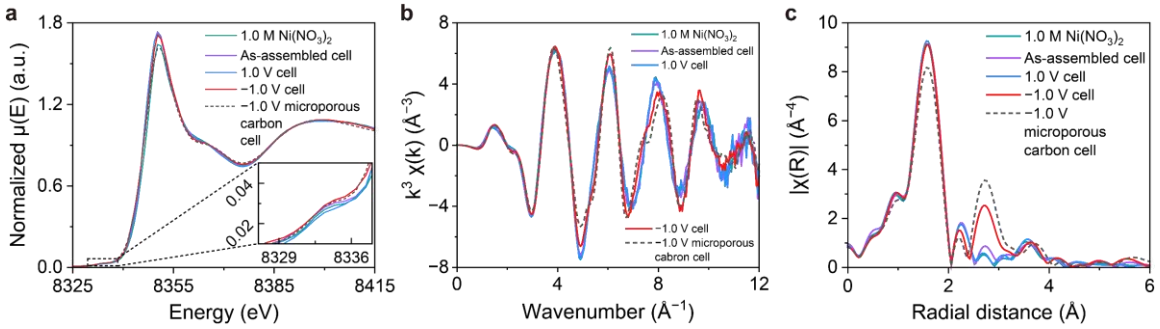

Figure S6. Association of Ni aqua ions in mesoporous carbon electrodes. Ni K edge a) normalized XANES spectra, b) $k^3\chi(k)$ spectra, and c) $|\chi(R)|$ spectra for 1.0 M $Ni(NO_3)_2$, as-assembled CMK-3 cell, CMK-3 cells at ±1.0 V, and XFP-01 cell at −1.0 V. The inset in (a) represents the zoomed pre-edge features. Mesoporous CMK-3 cell has smaller Ni–Ni scattering peak compared to microporous XFP-01 cell with similar edge step.

To examine the effect of spatial confinement on the oligomerization of Ni aqua ions, Ni K edge XAS was applied to supercapacitor cells with mesoporous CMK-3 as the active material and 1.0 M $Ni(OH)_2$ as the electrolyte. As demonstrated in Figure S6, the spectral features towards Ni–Ni coordination are lesser for mesoporous carbon cell than microporous carbon cell at −1.0 V, which indicate less structural change and thus weaker ion oligomerization. This is due to the larger average pore size and lack of micropores for the mesoporous carbon electrode, which thus cannot offer enough spatial confinement to the ions to form ionic oligomers. This result indicates the necessity of spatial confinement to the ion oligomerization.

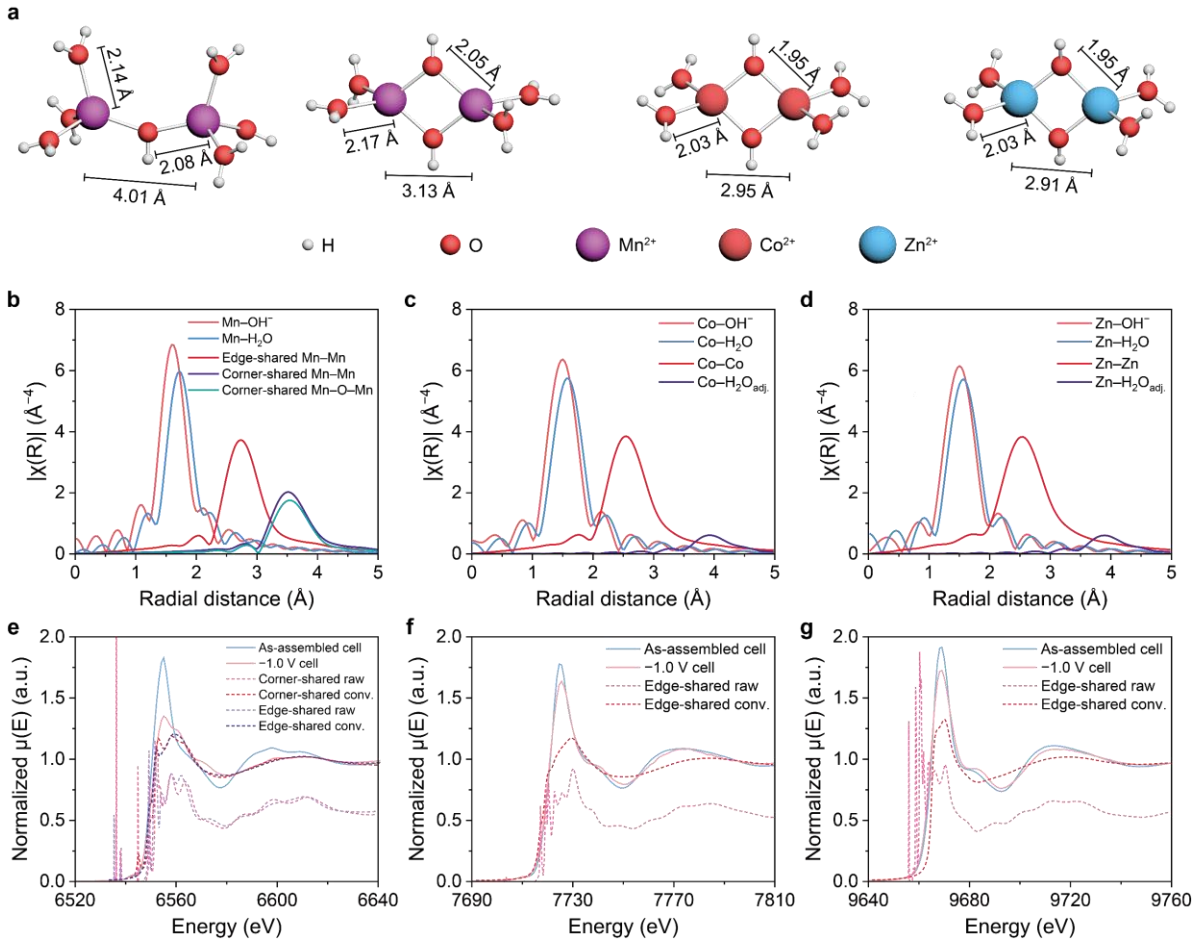

Figure S7. Theoretical analysis of Mn, Co, and Zn ionic oligomer structures upon association. a) DFT simulated structures of edge/corner-shared Mn ionic oligomers and edge-shared Co, Zn ionic oligomers with tetrahedral solvation structures (from left to right). b–d) Theoretical EXAFS |χ(R)| scattering peaks of the significant coordination shells for (b) Mn, (c) Co, and (d) Zn ionic oligomers. Co/Zn–$H_2O_{adj.}$ correspond to the scattering from O atoms in the H_2O molecules coordinated to the adjacent metal cation. e–g) Theoretical normalized μ(E) spectra of the DFT simulated (e) Mn, (f) Co, and (g) Zn ionic oligomers. The lower dash curves represent the calculated raw data, while the upper dash curves represent the convoluted spectra.

To analyze the spectral features obtained from the Mn, Co, and Zn K edge XAS measurements, DFT simulation, EXAFS calculation, and FDNMES calculation were used to model the ionic oligomers and their theoretical spectra. As shown in Figure S7, the best agreement between DFT calculations and experiment results is achieved by tetrahedral ionic oligomers with edge/corner hydroxo bridging. All the structures have well-matched features in their theoretical |χ(R)| spectra generated using Artemis software compared to the experimental result:[6] the M–H_2O peaks drop due to partial desolvation from six to four, which are also slightly broadened due to partial replacement of the H_2O with OH^- with a shorter coordination distance; the corner/edge-shared M–M packings generate scattering peaks around 2.7 Å and 3.6 Å. The results are rational considering the weak-field ligand nature of both H_2O and OH^-, which prefers tetrahedral coordination rather than planar square with higher crystal field splitting.

Nevertheless, the fitted tetrahedrons are not regular, instead are flattened to different extent, which together with the high discreteness of the oligomer mixture may explain the missing high pre-edge peak in the Mn and Co K edge XANES (Figure 2b, c). The optimized Mn–OH^- coordination distance is slightly longer than the experimental result, which is due to the noninvolvement of Jahn–Teller effect in the simulations.

Apart from $|\chi(R)|$ spectra, Mn, Co, and Zn K edge normalized $\mu(E)$ spectra of the optimized structures were also simulated using FDMNES package to compare to the experimental results.[4] The simulated results offer well-matched spectral features with the experimental results, including blunt white lines and suppressed oscillations after the white lines. The isosbestic points that mark the two-structure transition nature are also ideally met. The main disagreement between experimental and simulated spectra comes from small crests immediately after white lines, which are reproduced by the raw simulated spectra but smoothed out by the convoluted spectra.

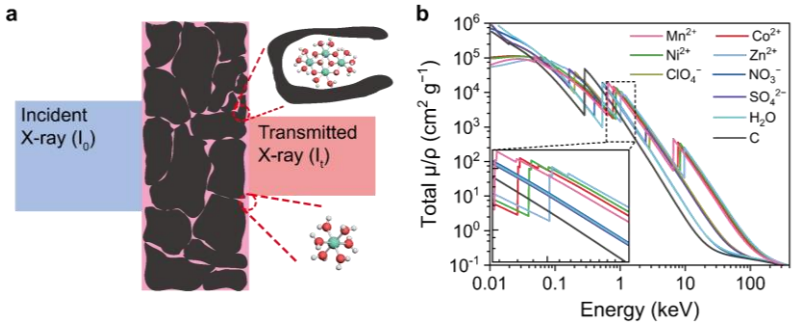

c

Electrolyte	Edge step	Thickness (μm mg^{-1})
$Mn(NO_3)_2$	0.347	30.990
$Co(NO_3)_2$	0.312	33.678
$Ni(NO_3)_2$	0.253	36.351
$Zn(NO_3)_2$	0.229	33.592

Figure S8. Estimation of the electrolyte thickness for edge step calculations. a) Scheme of the X-ray penetrating porous carbon electrode. The X-ray interacts with transition metal ions both inside carbon pores and within the vicinity between carbon particles, on the electrode surface, etc. b) X-ray mass attenuation coefficient of Mn^{2+}, Co^{2+}, Ni^{2+}, Zn^{2+}, NO_3^-, SO_4^{2-}, ClO_4^-, H_2O, and C.[11] Inset: zoomed feature in the energy range of transition metal K edge. c) Electrolyte thicknesses calculated using Equation S2 based on the edge step of as-assembled cells with different electrolytes, assuming a thorough infiltration and a uniform 1.0 M concentration in the electrodes.

As shown in Figure S8, while penetrating the working electrode, the X-ray interacts with transition metal ions both inside carbon micropores and in the vicinity of carbon particles, on the surface of the electrode, etc. As a result, the XAS spectrum collected is an average of the signal from both inside (solvated ions and ionic oligomers) and outside (solvated ions) carbon micropores. The X-ray adsorption of transition metal aqua ions can be identified from the total adsorption at and above their X-ray absorption edge energies due to the greatly increased absorption of these elements with relatively constant absorption of others. Apart from the species, the amount of transition metal aqua ions is proportional to the intensity of their XAS spectrum, which can be calculated from the edge step and electrolyte thicknesses using Equation S2. The electrolyte thickness can be estimated from the edge step of as-assembled cells with different electrolytes, assuming the electrolyte penetrates the as-assembled working electrode fully and maintain a uniform 1.0 M concentration throughout it. The calculation leads to estimated specific thickness of 30.990, 33.678, 36.351, and 33.592 μm mg^{-1} for Mn, Co, Ni, and Zn aqua ions, which are close to each other.

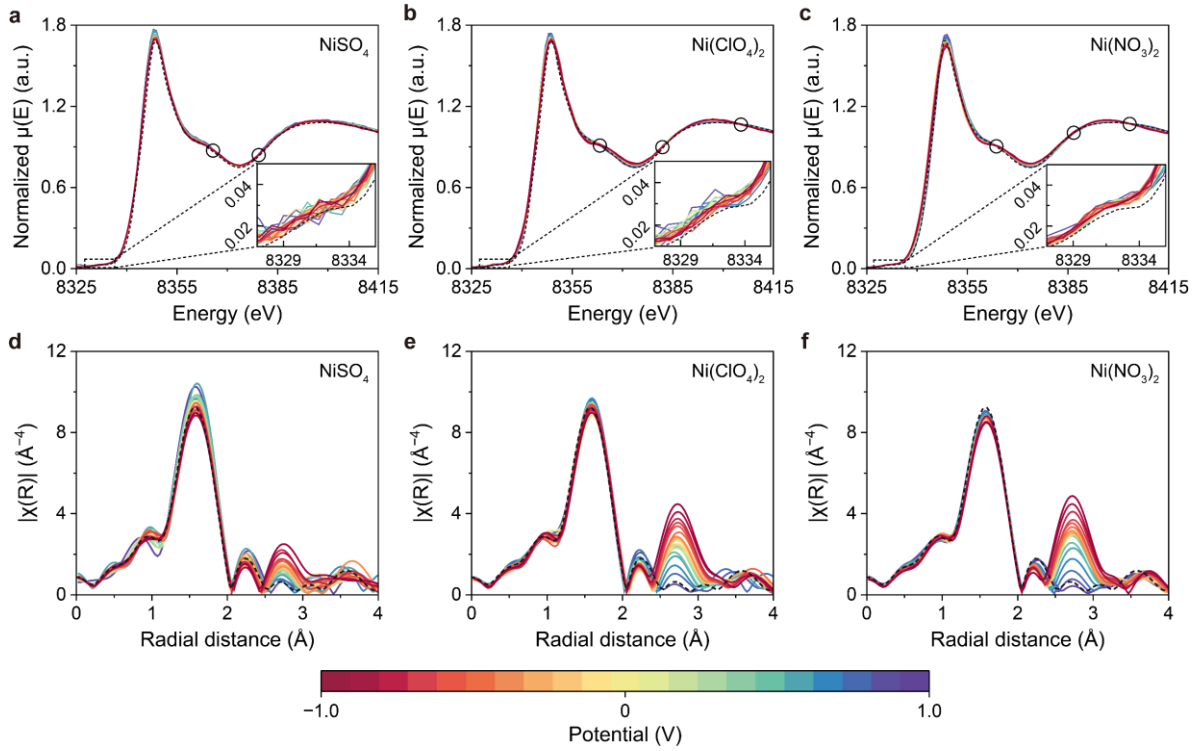

Figure S9. Anion-specific effect on the oligomerization of Ni aqua ions. a–c) Operando Ni K edge normalized μ(E) spectra of customized microporous carbon cells during chronoamperometry charging with 1.0 M (a) $NiSO_4$, (b) $Ni(ClO_4)_2$, and (c) $Ni(NO_3)_2$ electrolytes. The circuits highlight the isosbestic points. Inset: zoomed pre-edge features. d–f) The corresponding EXAFS |χ(R)| spectra of the cells. The dash curves represent the spectra of the electrolytes.

To analyze the effect of anion species on the oligomerization of transition metal aqua ions, we conducted Ni K edge XAS measurements on customized microporous carbon cells with electrolytes of different Ni salts. As shown in Figure S9, all the cells demonstrate constant Ni–O peak at 1.61 Å and varying Ni–Ni peak at 2.73 Å with potentials. The same coordination distances with different anions double confirm the origin of the spectral changes as the formation of Ni ionic oligomers, which keeps similar Ni–O coordination and introduces identical Ni–Ni coordinations independent of the anion used, rather than the formation of cation–anion pairing, which leads to different Ni–O coordinations and Ni–S/Cl/N coordinations depending on the coupling oxyanion. Nevertheless, the anions show effect on the degree of cation oligomerization that the height of Ni–Ni scattering peak, which is positively correlated to the coordination number, is different for different anions and follows the ranking of NO_3^- > ClO_4^- >> SO_4^{2-} due to different ion–ion and/or ion–pore interactions.[12] LCF of the normalized μ(E) spectra and edge step calculation (Figure 3) demonstrate the same ranking for the adsorption and oligomerization of Ni aqua ions. Nevertheless, the potential dependencies for the processes are almost the same with different anions, suggesting that the reaction barriers are not scattered and thus no direct involvement of the anions in the oligomerization process.

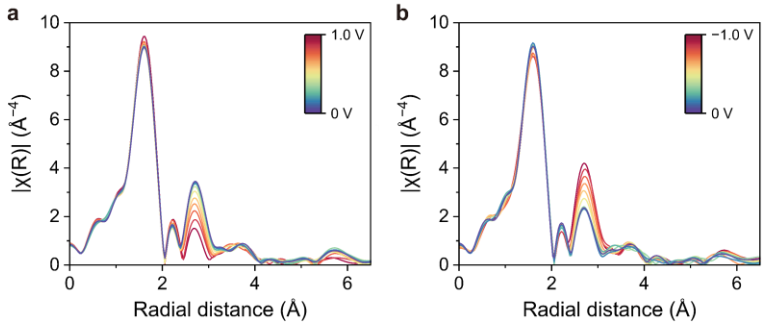

Figure S10. Reversible oligomerization of Ni aqua ions during the first CV charging processes. Selected Ni K edge |χ(R)| spectra of customized microporous carbon cells during the first (a) positive and (b) negative CV charging processes. The spectral changes are similar to the changes during chronoamperometry charging processes.

To compare the ion oligomerization process during CV and chronoamperometry charging, 10 spectra were selected from the first positive and negative CV charging at different points corresponding to 0–±1.0 V with 0.1 V step size (Figure S10). The spectral changes are very similar to the ones during chronoamperometry charging, that while the Ni–O peak keeps almost constant and the Ni–Ni peak at 2.73 Å raises/drops mainly after ±0.4 V, showing the same reaction barriers for the oligomerization. This indicates similar processes happen for both CV and chronoamperometry charging.

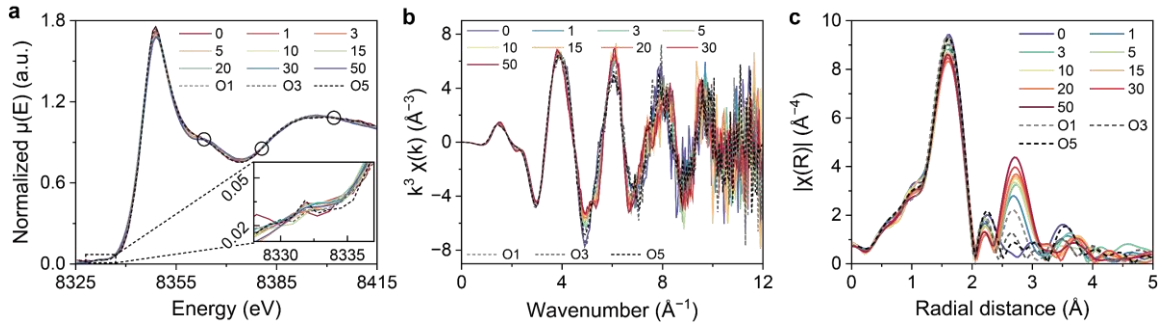

Figure S11. Accumulation of Ni ionic oligomers with cycling. Ni K edge a) normalized XANES spectra, b) $k^3\chi(k)$ spectra, and c) $|\chi(R)|$ spectra of customized microporous carbon cells after different cycles. O1, O3, and O5 represent the 1st, 3rd, and 5th opposite cycles. The circuits in (a) highlight the isosbestic points. The inset in (a) represents the zoomed pre-edge features.

Ni K edge XAS was applied to customized microporous carbon supercapacitors with 1.0 M $Ni(NO_3)_2$ electrolyte after different cycles (Figure S11). A clear migration of the spectra from Ni aqua ion to ionic cluster is observed in 50 negative cycles (0 to −1.0 V), which is especially obvious during the first 10 cycles. After the first 10 cycles, the spectra change less due to the gradual saturation of carbon micropores. During opposite cycles (O1 to O5, 0 to 1.0 V), the spectra shift gradually back to Ni aqua ion, indicating the destruction of ionic oligomers. LCF and edge step calculation of the spectra (Figure 5b) demonstrate that the portion of Ni aqua ion drops quickly from cycle 0 to 10 and mildly from cycle 10 to 50. Meanwhile, the concentration of Ni^{2+} also changes accordingly, indicating highly aligned ion adsorption and oligomerization. The composition and concentration shift back to the as-assembled state in 5 positive cycles, which suggests the evacuation of carbon micropores and revivification of their charge storage capability.

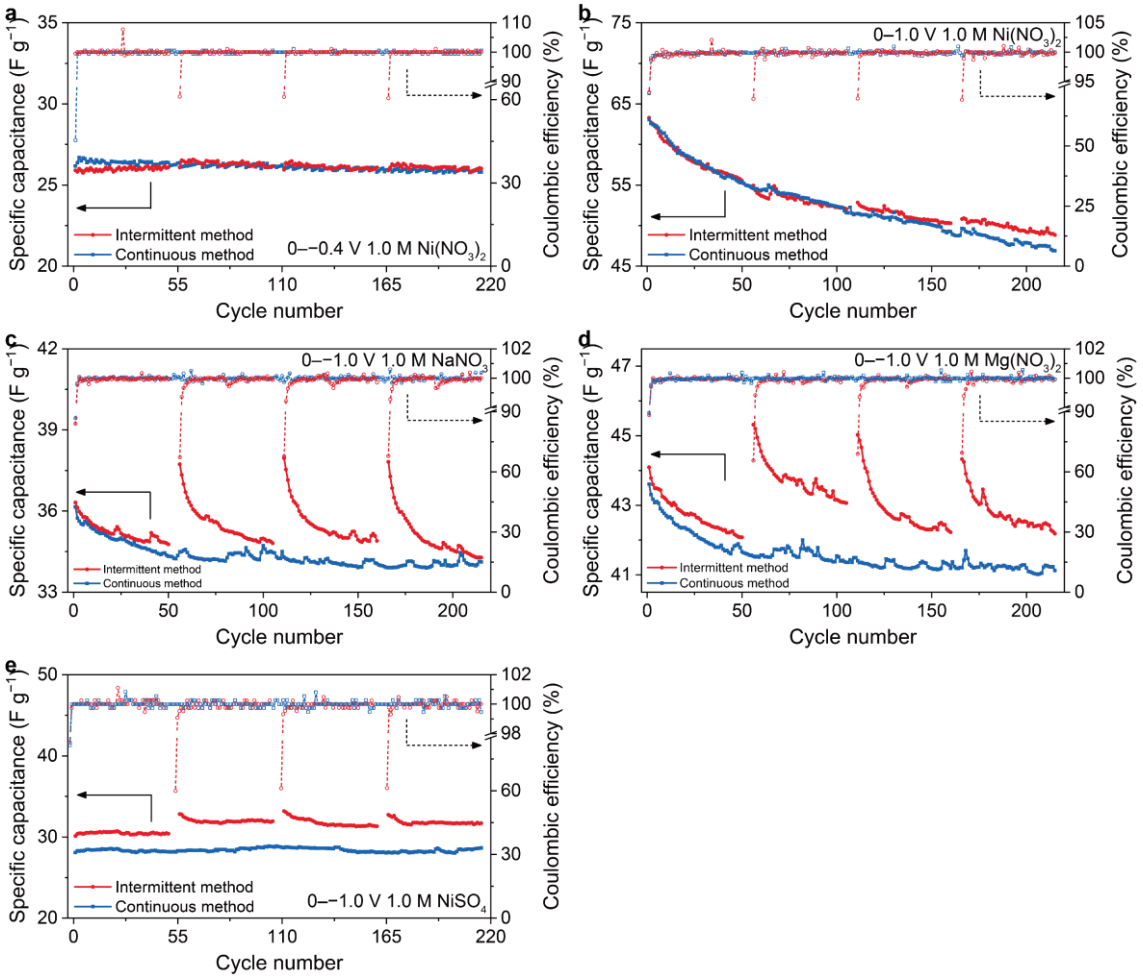

Figure S12. Cycling performance of customized microporous carbon cells with various metal aqua ion electrolytes. a, b) Specific capacitance of cells with 1.0 M $Ni(NO_3)_2$ electrolyte cycling between (a) 0 to −0.4 V and (b) 0 to 1.0 V. c, d) Specific capacitance of cells with 1.0 M (c) $NaNO_3$ and (d) $Mg(NO_3)_2$ electrolytes cycling between 0 to −1.0 V. e) Specific capacitance of cells with 1.0 M $NiSO_4$ electrolyte cycling between 0 to −1.0 V. Continuous cycling (blue) as well as intermittent cycling with 5 opposite cycles in between every 50 cycles (red) are used. For (a), (b), and (e), the latter shows no revivification effect, which is due to the lack of ion oligomerization and accumulation under these testing conditions and thus no ionic oligomer to destruct. For (c) and (d), intermittent reverse cycling shows the revivification effect, which implies similar ion accumulation and trapping for alkali and alkaline earth metal aqua ions to transition metal aqua ions, meanwhile proves the universality of our method.

To verify the effect of ion oligomerization and accumulation on energy storage, the capacitance retention of customized microporous carbon cells with Ni aqua ions under various conditions are analyzed. Firstly, as shown in Figure S12, there is negligible capacitance fading when the cell is cycled between 0 to −0.4 V. The cell maintains a stable specific capacitance around 26 F g^{-1} for 200 cycles with both continuous method and intermittent method. This is because that within this potential range, Ni aqua ions do not associate and accumulate according to the operando XAS result. As such, there is neither capacitance contribution from ion oligomerization nor capacitance fading due to accumulation of ionic oligomers.

Secondly, when cycled positively between 0 to 1.0 V, the capacitance fades quickly from 63 F g^{-1} to 47 F g^{-1} in 200 cycles, but intermittent cycling has no revivification effect. This is due to the missing of ionic oligomers in the negative electrode (counter electrode during positive cycling) due to its less voltage share (less than 0.4 V, as shown in Figure S2), which is insufficient for intensive ion oligomerization. As a result, there are not many ionic oligomers to release from the counter electrode and the revivification effect is not observed. The capacitance fading during positive cycling should come mainly from irreversible side reactions.

To examine the effect of intermittent reverse cycling in general on metal aqua ions, we measure the cycling performance of customized microporous carbon cells with 1.0 M $NaNO_3$ and $Mg(NO_3)_2$ electrolytes. Both cells demonstrate capacitance fading cycling between 0 to −1.0 V with continuous cycling, which is especially obvious during the first 50 cycles, which implies similar ion accumulation and trapping for alkali and alkaline earth metal aqua ions. With intermittent reverse cycling, the capacitance is restored to the initial level after 5 cycles of opposite charging/discharging and fades again for the new cycling. The same revivification effect as for transition metal aqua ions proves the universality of our cycling strategy, providing guidance for the development of advance electrochemical energy storage and water treatment technologies.

Since SO_4^{2-} promotes ion oligomerization less than other anions (Figure 3 and Figure S9), using SO_4^{2-}-based electrolyte is another strategy to reduce capacitance fading from the accumulation of ionic oligomers. Indeed, no capacitance fading is observed for the cell with $NiSO_4$ electrolyte cycling between 0 to −1.0 V. However, $NiSO_4$ electrolyte also brings smaller specific capacitance compared to $Ni(NO_3)_2$ electrolyte at 0.5 mA current, which is likely due to the reduced ion adsorption and oligomerization and is disfavored for the purpose of energy storage. Further studies should focus on advanced electrolytes with simultaneous high specific capacitance and less ion accumulation inside carbon micropores.

References

[1] a) G. Kresse, J. Furthmüller, *Comput. Mater. Sci.* **1996**, *6*, 15; b) G. Kresse, J. Furthmüller, *Phys. Rev. B* **1996**, *54*, 11169.

[2] P. E. Blöchl, *Phys. Rev. B* **1994**, *50*, 17953.

[3] J. P. Perdew, K. Burke, M. Ernzerhof, *Phys. Rev. Lett.* **1997**, *77*, 3865.

[4] Y. Joly, *Phys. Rev. B* **2001**, *63*, 125120.

[5] O. Bunău, Y. Joly, *J. Phys. Condens. Matter* **2009**, *21*, 345501.

[6] B. Ravel, M. Newville, *J. Synchrotron Radiat.* **2005**, *12*, 537.

[7] K. S. W. Sing, D. H. Everett, R. A. W. Haul, L. Moscou, R. A. Pierotti, J. Rouquérol, T. Siemieniewska, *Pure Appl. Chem.* **1985**, *57*, 603.

[8] C. Prehal, C. Koczwara, N. Jackel, A. Schreiber, M. Burian, H. Amenitsch, M. A. Hartmann, V. Presser, O. Paris, *Nat Energy* **2017**, *2*, 16215.

[9] a) Z. Weng, F. Li, D.-W. Wang, L. Wen, H.-M. Cheng, *Angew. Chem. Int. Ed.* **2013**, *52*, 3722; b) B. Evanko, S. J. Yoo, S.-E. Chun, X. Wang, X. Ji, S. W. Boettcher, G. D. Stucky, *J. Am. Chem. Soc.* **2016**, *138*, 9373.

[10] a) X. P. Wang, H. J. Wu, S. B. Xi, W. S. V. Lee, J. Zhang, Z. H. Wu, J. O. Wang, T. D. Hu, L. M. Liu, Y. Han, S. W. Chee, S. C. Ning, U. Mirsaidov, Z. B. Wang, Y. W. Zhang, A. Borgna, J. Wang, Y. H. Du, Z. G. Yu, S. J. Pennycook, J. M. Xue, *Energy Environ. Sci.* **2020**, *13*, 229; b) X. Wang, S. Xi, W. S. V. Lee, P. Huang, P. Cui, L. Zhao, W. Hao, X. Zhao, Z. Wang, H. Wu, H. Wang, C. DIao, A. Borgna, Y. Du, Z. G. Yu, S. Pennycook, J. M. Xue, *Nat. Commun.* **2020**, *11*, 4647; c) L. Wang, X. Wang, S. Xi, Y. Du, J. Xue, *Small* **2019**, *15*, 1902222.

[11] C. T. Chantler, K. Olsen, R. A. Dragoset, J. Chang, A. R. Kishore, S. A. Kotochigova, D. S. Zucker, NIST, Physical Measurement Laboratory, **1995, 1996, 2001 ed.**

[12] a) D. Schröder, L. Ducháčková, J. Tarábek, M. Karwowska, K. J. Fijalkowski, M. Ončák, P. Slavíček, *J. Am. Chem. Soc.* **2011**, *133*, 2444; b) R. N. Collins, K. M. Rosso, A. L. Rose, C. J. Glover, T. D. Waite, *Geochim. Cosmochim. Acta* **2016**, *177*, 150; c) J. P. Chen, M. Lin, *Carbon* **2001**, *39*, 1491; d) M. K. Doula, A. Ioannou, *Microporous Mesoporous Mater.* **2003**, *58*, 115; e) J. W. Lee, J. M. Ko, J.-D. Kim, *J. Phys. Chem. C* **2011**, *115*, 19445; f) P. Lo Nostro, B. W. Ninham, *Chem. Rev.* **2012**, *112*, 2286.